



IZMIR DEMOCRACY UNIVERSITY

NATURAL & APPLIED SCIENCES JOURNAL

IDUNAS

E-ISSN: 2645-9000

Year: 2018

Volume: 1, Issue: 2

Red Blood Cell Analysis by Hyperspectral Imaging

Hüseyin Kurtuldu*¹ , Aynur Didem Oktan¹ , Hatice Candan¹ , Beste Sahra Cihangiroğlu¹ 

Abstract

Hyperspectral imaging is a new technology that aims to use the spectral information of each pixel in different spectral bands to find, identify and classify objects in an image. The hyperspectral imaging system, which is frequently used in the field of remote sensing, is becoming a new imaging model for medical applications and non-invasive disease diagnosis. In this study, a hyperspectral microscope system capable of capturing images of biological samples at different range of spectral wavelengths was developed. With this system, red blood cells in the blood sample were analyzed at various wavelengths and image classification was performed to determine the locations of red blood cells (erythrocytes). Subsequently, the detection of cytoplasm, cell edge, extracellular fluid, and pale area in the cell center of each erythrocyte was successfully performed.

Keywords

Hyperspectral imaging, red blood cell, classification, segmentation, spectral bands

¹ Department of Biomedical Engineering Başkent University

*Corresponding Author: hkurtuldu@baskent.edu.tr

Manuscript received date: July 11, 2018

Accept Date: November 27, 2018

Published Date: December 31, 2018.

1. INTRODUCTION

Blood analysis is one of the most commonly used diagnostic techniques in healthcare. Most microscope-based high-tech systems frequently require blood smearing and evaluation by a pathologist for definitive designation of blood diseases [1]. Anemia, the blood hemoglobin value below the level determined by the World Health Organization [2], causes tissue hypoxia by reducing the oxygen-carrying capacity of blood. The diagnosis of anemia made with the naked eye under a microscope depends on the experience of the individual. For this reason, it is important to develop systems that will eliminate the human factor in such diagnoses.

Three different types of cells are usually imaged in microscopic analyzes leukocytes, erythrocytes, and platelets. The hemoglobin (Hb) concentrations of the blood smear as well as the leukocyte, platelet and erythrocyte counts are also examined when anemia is diagnosed. Erythrocytes are cells that take oxygen from the lungs and transport them to tissues and organs through the Hb protein for the body and organs. They do not contain mitochondria or nuclei when they mature. The cells are about $7.5 \mu\text{m}$ in diameter and have a thickness at the thickest point of $2.0 \mu\text{m}$ and a minimum thickness of $1 \mu\text{m}$ in the center. Due to their bi-concave structures, the central part of the erythrocyte cell appears paler in the microscopic examination than in the other areas. The ratio of the diameter of this region to the cell diameter is one of the methods used to determine the amount of hemoglobin. Normally, this ratio is $1/3$. As it decreases, the amount of tissue hypoxia increases. When the ratio is $1/2$, it is termed + hypochromia. If the ratios are $2/3$ and $3/4$, they are then called ++ hypochromia and +++ hypochromia, respectively. As the diameter of the pale area is very close to the erythrocyte cell diameter, it is named ++++ hypochromia. The correct determination of this ratio is critical for accurate diagnosis [3].

Several methods have previously been applied for blood cell segmentation, including the separation of blood cells into leukocytes and erythrocytes. Sharif et al. [4] provided a method for automatic erythrocyte count. This method included Ycber color transformation, masking, and morphological operations with a watershed algorithm. Chourasiya and Rani [5] proposed an efficient and cost-effective computer-based imaging system that performs analysis to automate erythrocyte counting. This technique employed a masking method to identify individual leukocytes and distinguish overlapping ones in the blood sample. Wang et al. [6] visualized blood cells by a scanning electron microscope. Individual cells were extracted using a contour

guiding method, and the variation of each pixel on a cell image was used to obtain the three-dimensional shape information. Guan et al. [7] used a new method based on hyperspectral imaging for pathological leukocyte segmentation. This technique was used to capture one-dimensional spectral and two-dimensional spatial information of leukocytes. The imaging system consisted of a CCD camera to capture images in a light microscope, an acousto-optic tunable filter for wavelength selection, a computer for analyzing images and spectral curves. By applying a spectral sorting algorithm, leukocytes were divided into four groups at a wavelength range of 550 to 950 nm. Wu et al. [8] offered a gray level-based method that can only detect nuclei to segment leukocytes. Another method proposed by Liao and Deng [9] was limited to multicolored leukocyte cells and, in practice, gave good results in circular leukocyte cells. On the other hand, the two neural network-based methods presented by Yi et al. [10] did not distinguish between the nucleus and the cytoplasm, as they performed well in detecting leukocytes [10]. Until now, there has been no study on the segmentation of erythrocyte cells via hyperspectral imaging.

In this study, to the best of the authors' knowledge, a hyperspectral microscopic imaging system capable of capturing images of blood smear at different spectral wavelengths was used for the first time to determine the location, cytoplasm, cell edge, extracellular fluid and the pale area of erythrocytes. This study suggests that hyperspectral imaging can be used as a useful tool to diagnose blood diseases such as anemia.

2. MATERIALS & METHOD

2.1 Hyperspectral imaging system

Hyperspectral imaging measures the intensity of light reflected or transmitted from illuminated materials in a wide range of wavelengths from visible to infrared. The spectral signature of each pixel is obtained for finding, recognizing, and rating objects in an image. Since each material has its own signature, it is possible to separate objects from each other [11, 12]. Hyperspectral imaging is becoming a technology used in a wide range of geology, chemistry, medicine, agriculture, forestry, biomedical, space-planet research, and military applications for defense and security purposes [13, 14].

In this study, blood smear samples were examined with an upright Olympus microscope at 100X magnification. A liquid crystal tunable filter (LCTF) attached to a CMOS camera was integrated into the microscope to obtain hyperspectral images. A halogen light source was used for illumination. The block diagram of the system components as well as the microscope system are shown in Figure 1. The LCTF was used to set the wavelength between 420 and 730 nm, and the camera was used to capture gray scale images at the desired wavelength. The camera's exposure (the amount of light reaching the sensor) and gain values (the amplification of the sensor signal) were adjusted to optimize the intensity level of the images for different ranges of wavelength. Increasing the exposure time allows the sensor to collect more light.

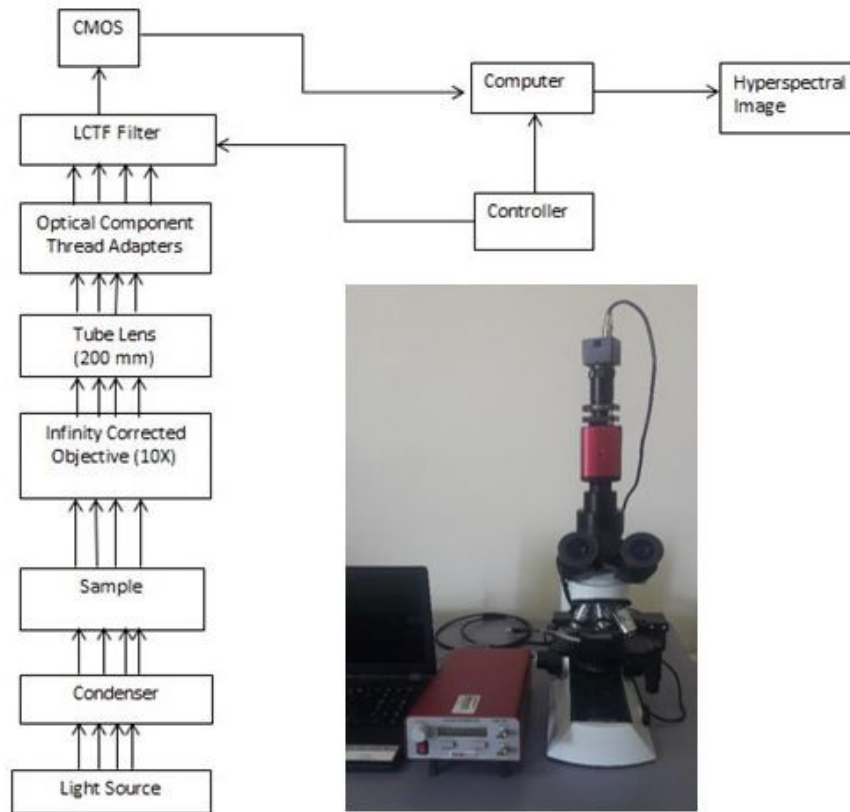


Figure 1. Block diagram of the components for hyperspectral microscope system.

2.2 Acquisition

In the range of 500-690 nm with 10 nm increments, 20 different images of the sample were captured (Figure 2). During the acquisition, gain was kept constant (1/10 dB) and four exposure values were determined between 500 and 690 nm. As listed in Table 1, the exposure value was set to 0.325 s for the wavelength range of 500-530 nm, 0.167 s for 540-570 nm, 0.125 s for 580-600 nm, and 0.100 s for 610-690 nm. Since the halogen source produces a more intense light in the infrared portion of the spectrum, the exposure value decreases with increasing wavelength.

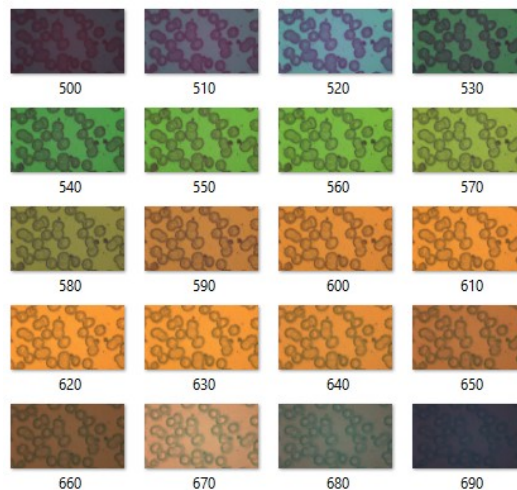


Figure 2. Hyperspectral images of the blood sample captured between 500 and 690 nm with an increment of 10 nm.

Table 1. Exposure values of the camera for different wavelength ranges.

Wavelength (nm)	Exposure (s)
500 – 530	0,325
540 – 570	0,167
580 – 600	0,125
610 – 690	0,100

2.3 Preprocessing

Background subtraction was applied to the raw images to compensate for uneven illumination and image artifacts due to optical components in the system. A gray-scale image of the cover-glass blood smear captured at 600 nm is shown in Figure 3(a). A background image taken on an empty cover-glass at the same wavelength is delineated in Figure 3(b). The images were passed through a Gaussian filter with a 7x7 scan window to reduce noise. The image was normalized by the background after being extracted from the background image. The background-removed blood image is represented in Figure 3(c). A similar procedure was applied to all images captured between 500 and 690 nm.

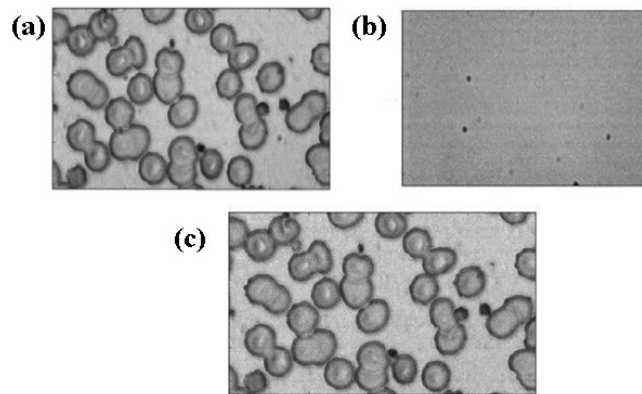


Figure 3. (a) Raw image of the cover-glass blood smear at 600 nm, (b) background image of an empty cover-glass, (c) background subtracted image of the blood smear

2.4 Classification

23 different regions of interest in the vicinity of individual erythrocyte cells were selected in blood smear images for classification (Figure 4(a)). Four regions, the central region of erythrocytes (Region-1), cytoplasm (Region-2), cell margins (Region-3), and extracellular fluid (Region-4) were identified for each cell (Figure 4(b)). Figure 5 delineates how the spectral intensity changes between 500 and 660 nm for these four regions of a single cell. The extracellular region transmits more light than the other regions below 610 nm while the pale region absorbs less light than the extracellular area above this wavelength. The cell edge has a similar absorbance throughout the wavelength range and the cytoplasm has a transmittance peak at about 570 nm. Images captured above 660 nm were not used in the classification due to defocusing caused by chromatic aberration and insufficient light. 23 individual erythrocyte cells in blood smear images were selected for classification in these wavelengths.

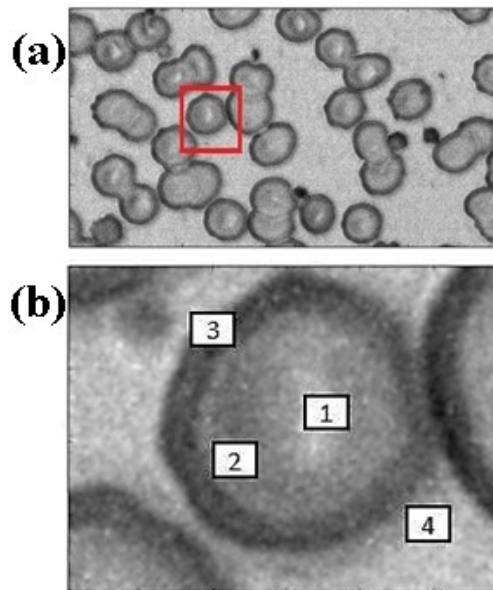


Figure 4. (a) An individual erythrocyte cell selected for analysis (b) identification of the regions- 1) pale area 2) cytoplasm, 3) cell edge, and 4) extracellular fluid.

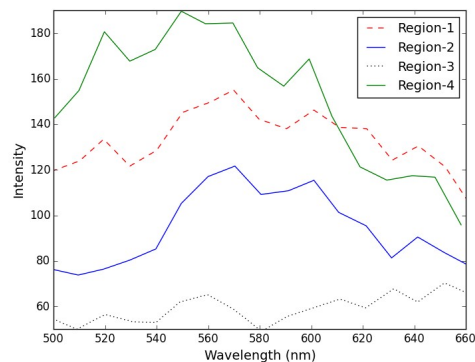


Figure 5. For the regions (Region 1, 2, 3 and 4) shown in Figure 4(b), spectral intensity as a function of wavelength.

Support Vector Machines (SVM), a set of supervised machine learning methods, was employed to determine the optimal level of separation between the regions [15, 16]. 10 of the 23 erythrocyte cells were used as training data and the remaining 13 were utilized as test data. For a total of 17 wavelengths separated by 10 nm, the intensity ranges were determined by considering the pixel values and standard deviations of the four regions within each cell. These ranges were trained in the SVM classifier. The classification was performed pixel by pixel for the region of interest. After the training, the classifier in the selected wavelength predicts which class (region 1, 2, 3, 4) each pixel in the region belongs to. Increasing the number of training and test samples is expected to increase the performance of classification models.

3. RESULTS

Figure 6 shows the result of classifying one of the 13 cells selected for testing. The colors assigned to Region-1 (pale area), Region-2 (cytoplasm), Region-3 (cell edge), and Region-4 (extracellular fluid) are black, dark blue, pink, and white, respectively. Not a single wavelength was sufficient to detect all regions at the same time, so the classification of multiple wavelengths was necessary. While the wavelength between 520 and 540 nm is more suitable for detecting the pale area, the range of 550 to 630 nm is better for identifying the extracellular fluid region.

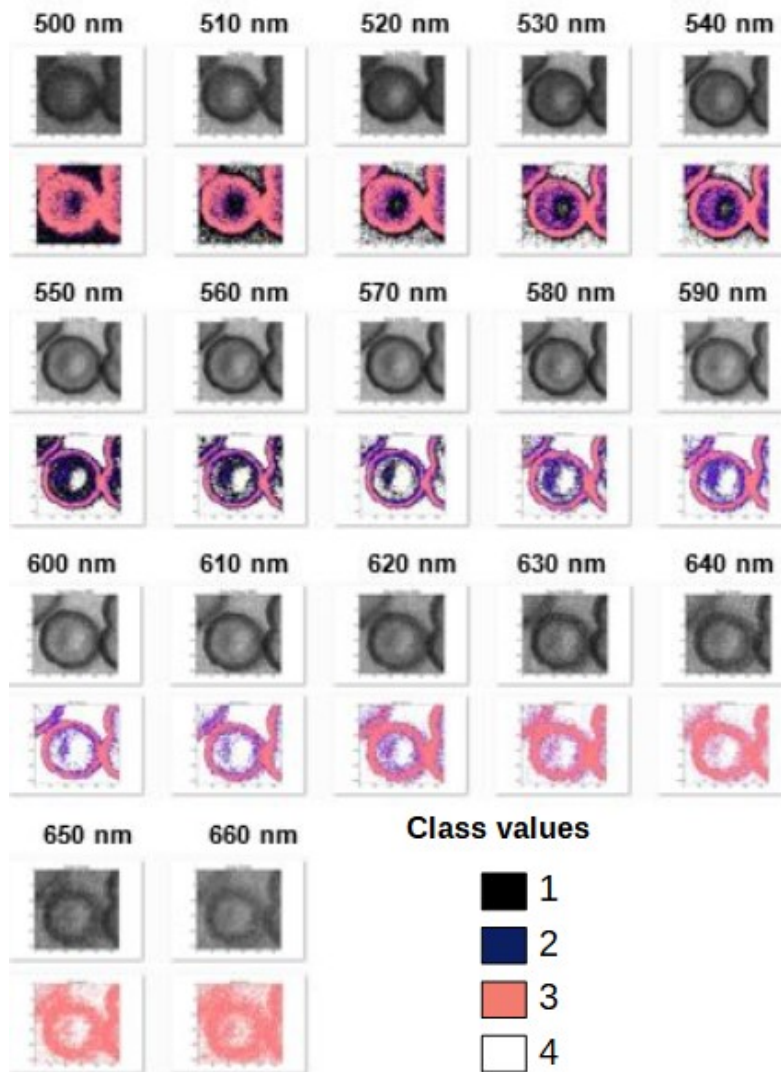


Figure 6. Classification of a cell in a region of interest based on the values Region-1) pale area 2) cytoplasm, 3) cell edge, and 4) extracellular fluid.

The performance of the test with 13 cells was measured by sensitivity and specificity. Test sensitivity is the ability of a test to identify the regions accurately with the assigned region number (true positive rate), whereas the test specificity is the ability of the test to correctly identify those without the appointed number (true negative rate) At the range from 520 to 540 nm, the central region 1 and the region 2 with cytoplasm were detected with 49.7 % and 33.4 % sensitivity, and 56.8 % and 36.3 % specificity, respectively. The region of cell margin had a sensitivity of 90.3 % and specificity of 98.1 % in the range of 550-590 nm. The fourth segment, extracellular fluid fraction, was predicted between wavelengths of 550 and 630 nm with 96.3 % sensitivity and 96.6 % specificity. The accuracies of classification were 53.8 %, 38.4 %, 92.3 %, and 92.3 % for Region-1, 2, 3, and 4, respectively.

4. DISCUSSION AND CONCLUSION

In this study, we proposed a hyperspectral microscopic imaging system capable of capturing images of blood smear over wide range of spectral wavelengths. A classifier method trained with intensity images of different wavelengths was used to identify the cytoplasm, the border and the pale area of erythrocyte cells as well as the region of extracellular fluid.

The analysis of erythrocyte cells is important in the diagnosis of anemia, where the level of hypochromia is generally determined by the diameter of the pale area and that of the cells. This method is usually performed by a pathologist, so it is prone to human error. Accurate determination of the level affects the treatment to follow [17]. In this study, we proposed a hyperspectral analysis method that could be used to automate this diagnostic process. In this technique, the border defining the cell pixels was detected with high accuracy. We showed that imaging at wavelengths between 520 and 540 nm is best for

distinguishing the number of pixels in the pale area and the pixels belonging to the erythrocyte cell. Training the classifier with more cells will increase the accuracy of the detection of the pale region. Accuracy can also be increased by using a fixed, high transmission band-pass filter in this wavelength range, rather than a tunable filter with a relatively low transmittance.

In clinical applications, the hyperspectral microscopic imaging method can be used to determine the level of hypochrome after the peripheral smear of blood samples from patients. In this way, errors due to the human factor could be eliminated in diameter measurement.

Extracellular fluid contains ions such as sodium, chlorine, and potassium. These ions provide acid-base balance by intracellular osmotic pressure. Hyponatremia and hypernatremia are related to the amount of sodium ion. Sodium has an emission at about 589 nm [18]. The hyperspectral system, which can detect the extracellular fluid region with accuracy above 90 % at 550-630 nm, could also be used to obtain the spectral intensity as a function of the amount of sodium present in this fraction of the cell.

References

- [1] M. F. Özçelik and H. Ş. Bilge, "The determination of white blood cell borders with using of logical and morphological operations in microscopic blood images," in *Signal Processing and Communications Applications Conference (SIU), 2010 IEEE 18th*. IEEE, 2010, pp. 688–691.
- [2] N. Altın, M. Koray, S. E. Meseli, and H. Tanyeri, "Oral manifestations of anemia," *CLINICAL AND EXPERIMENTAL HEALTH SCIENCES*, vol. 6, no. 2, pp. 86–92, 2016.
- [3] İ. AYDOĞDU, "Hastalıkta ve sağlıkta kan hücreleri," *Türkiye Klinikleri Journal of Hematology Special Topics*, vol. 5, no. 4, pp. 16–27, 2012.
- [4] J. M. Sharif, M. Miswan, M. Ngadi, M. S. H. Salam, and M. M. bin Abdul Jamil, "Red blood cell segmentation using masking and watershed algorithm: A preliminary study," in *Biomedical Engineering (ICoBE), 2012 International Conference on*. IEEE, 2012, pp. 258–262.
- [5] S. Chourasiya and G. U. Rani, "Automatic red blood cell counting using watershed segmentation," *Hemoglobin*, vol. 14, p. 17, 2014.
- [6] R. Wang, B. MacCane, and B. Fang, "Rbc image segmentation based on shape reconstruction and multi-scale surface fitting," in *Information Science and Engineering (ISISE), 2010 International Symposium on*. IEEE, 2010, pp. 586–589.
- [7] Y. Guan, Q. Li, H. Liu, Z. Zhu, and Y. Wang, "Pathological leucocyte segmentation algorithm based on hyperspectral imaging technique," *Optical Engineering*, vol. 51, no. 5, p. 053202, 2012.
- [8] J. Wu, P. Zeng, Y. Zhou, and C. Olivier, "A novel color image segmentation method and its application to white blood cell image analysis," in *Signal Processing, 2006 8th International Conference on*, vol. 2. IEEE, 2006.
- [9] Q. Liao and Y. Deng, "An accurate segmentation method for white blood cell images," in *Biomedical Imaging, 2002. Proceedings. 2002 IEEE International Symposium on*. IEEE, 2002, pp. 245–248.
- [10] F. Yi, Z. Chongxun, P. Chen, and L. Li, "White blood cell image segmentation using on-line trained neural network," in *Engineering in Medicine and Biology Society, 2005. IEEE-EMBS 2005. 27th Annual International Conference of the*. IEEE, 2006, pp. 6476–6479.
- [11] P. Shippert, "Introduction to hyperspectral image analysis," *Online Journal of Space Communication*, vol. 3, 2003.
- [12] S. V. Panasyuk, S. Yang, D. V. Faller, D. Ngo, R. A. Lew, J. E. Freeman, and A. E. Rogers, "Medical hyperspectral imaging to facilitate residual tumor identification during surgery," *Cancer biology & therapy*, vol. 6, no. 3, pp. 439–446, 2007.
- [13] T. H. Kosanke, S. E. Perry, and R. Lopez, "High-resolution hyperspectral imaging technology: Implications for thin-bedded reservoir characterization," 2017.
- [14] L. Khaodhiar, T. Dinh, K. T. Schomacker, S. V. Panasyuk, J. E. Freeman, R. Lew, T. Vo, A. A. Panasyuk, C. Lima, J. M. Giurini *et al.*, "The use of medical hyperspectral technology to evaluate microcirculatory changes in diabetic foot ulcers and to predict clinical outcomes," *Diabetes care*, vol. 30, no. 4, pp. 903–910, 2007.
- [15] O. Sezer, A. Erçil, and M. Keskinöz, "Independent component based 3d object recognition using support vector machines," in *Signal Processing and Communications Applications Conference, 2005. Proceedings of the IEEE 13th*. IEEE, 2005, pp. 99–102.
- [16] G. Mercier and M. Lennon, "Support vector machines for hyperspectral image classification with spectral-based kernels," in *Geoscience and Remote Sensing Symposium, 2003. IGARSS'03. Proceedings. 2003 IEEE International*, vol. 1. IEEE, 2003, pp. 288–290.

- [17] B. Turgut, “How important is anemia for the clinician?” *Balkan Medical Journal*, vol. 2010, no. 1, 2010.

The Effect of Constant Magnetic Fields on Programmable Shunts

Hüseyin Kurtuldu*¹ , Büşra Özgöde¹ 

Abstract

The valve pressure settings of the programmable shunt valves may be changed undesirably in the high magnetic field environments, and in many cases, these changes are not noticeable. Recent studies have shown that this effect increases in parallel with the increasing diversity of permanent magnet containing devices used in daily life. In this study, the effects of the non-ionizing magnetic field produced by devices such as smartphones and headphones on the programmable cerebral shunts were investigated. One of the programmable valves, frequently preferred in the treatment of hydrocephalus, was used in this study. First, the minimum magnetic flux densities that could affect these valves when exposed to an external magnetic field have been determined. Then, the effect of the magnetic flux densities produced by two different earphones and a mobile phone on this valve was investigated. It has been observed that such external magnetic fields can cause undesirable pressure changes on the valves at close distances, and these results suggest that patients should be aware of this effect.

Keywords

Hydrocephalus, Programmable Shunts, Magnetic Effect

¹ Department of Biomedical Engineering Başkent University

*Corresponding Author: hkurtuldu@baskent.edu.tr

Manuscript received date: June 21, 2018

Accept Date: August 13, 2018

Published Date: December, 2018.

1. INTRODUCTION

Hydrocephalus develops as a result of cerebrospinal fluid (CSF) accumulation in ventricles due to the imbalance between the production and absorption of CSF [1]. Since it is not possible to restore the circulation of CSF in the most of the patients, the transfer of fluid from the brain to another body cavity is provided by the systems called shunts. Various shunt types are used in neurosurgical applications. The most preferred of these are the conventional constant pressure shunts and programmable shunts. The pressure settings of the programmable shunt valves can be performed without any surgical or interventional procedure considering the clinical and radiological findings of the patient. The pressure settings of these valves, which are regulated by the magnetic field principle, may vary undesirably and are not mostly noticeable in the high magnetic field environments [2–6, 6–11].

Many studies in the literature show that unwanted opening pressure changes in the programmable valves occur most frequently during MR imaging [12, 13]. However, in parallel with the increase in the diversity of devices used in our daily lives, it has been reported that different devices, besides MR imaging, performed this effect in the studies especially in the recent years.

In this study, the effects of the non-ionizing constant magnetic field, produced by devices such as smartphones and headphones, on the programmable cerebral shunts were investigated. According to the measurements of the magnetic flux density, it is seen that the magnetic fields of the shunt valves of these devices are at the levels that can change the pressure settings. For that reason, patients and their relatives should bear in mind that the devices that produce high magnetic fields on the shunt surface may cause undesirable pressure changes in the shunts.

2. MATERIALS & METHOD

One of the frequently used programmable valves in neurosurgery was selected for the study. The valve can be adjusted to 8 different performance levels, and it is possible to optically measure the performance properties of the valve opening press without requiring a radiological evaluation by means of the transparent layer on the magnets and revolving structure in the shunt. The valve was adjusted to 8 different performance levels to obtain shunt mechanism images by using the zoom-lens camera system (Figure 1). As delineated in the Figure-1, the angles between the tantalum ball-bearing magnet and the fixed reference point are measured according to 8 different performance levels.

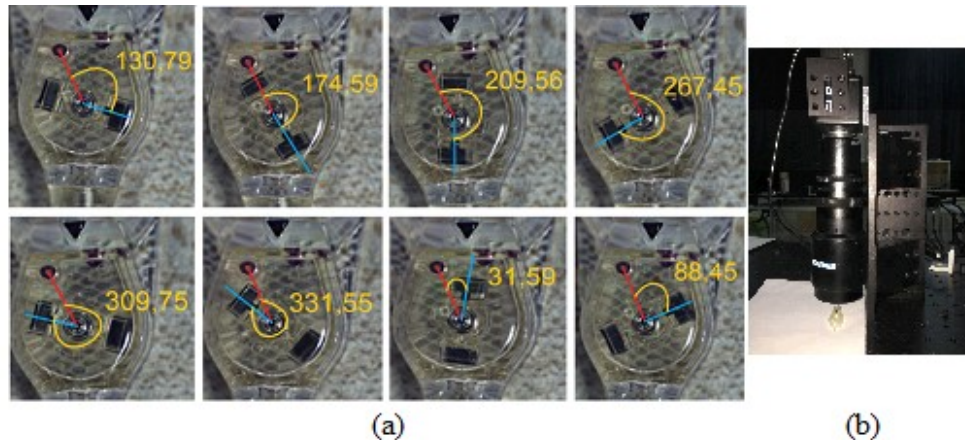


Figure 1. (a) Images taken using the zoom lens at different performance levels of the valve (b) Zoom-lens camera device

After calculating the angles in the images without the effect of any magnetic field, the valve was exposed to 30 Gauss (G) and 90 G magnetic fields using permanent magnets and the change in the angles at different performance levels were determined. In this study, magnetic field measurements were carried out with a Hall Effect sensor (Honeywell SS49E) to observe the effect of magnetic field created by devices with permanent magnets such as headphones and mobile phones. A scanning system consisting of three-dimensional micro-sensitive translation stages (Psaron HTI) were employed for these measurements. The sensor was mounted on the scanning system and the motion and the sensor are synchronized to measure the magnetic field around the object to be scanned.

The three-dimensional scanning, with the sensor layer mounted on the micro-sensitive stages as indicated in Figure-2, was first performed for the headphone from 1 mm to 7 mm from the surface with 1 mm steps. Similarly, the phone surface is scanned by a movement from 1 mm to 8 mm with 0.5 mm steps. The magnetic flux density measurements were performed by scanning laterally (x-y plane) the selected regions of iPhone 6 Plus, placed under the sensor at different heights (z-axis). A smartphone (iPhone 6 Plus) and 2 different headphones (Apple EarPods and Philips SHE1350) have been tested for this study.

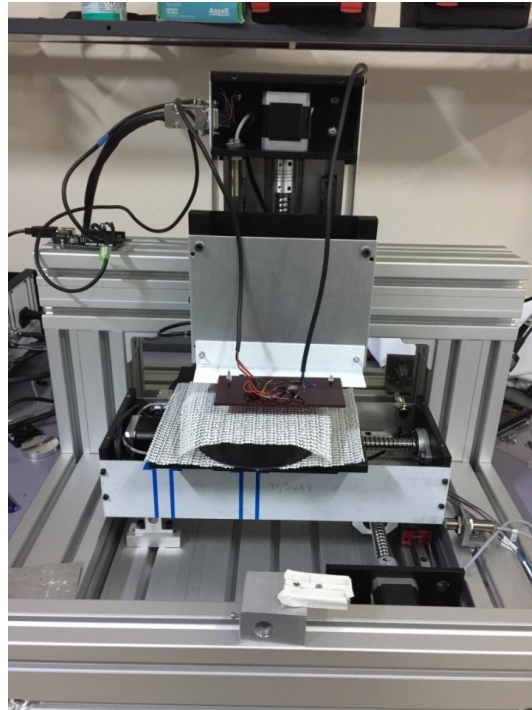


Figure 2. The three-dimensional measurement system with micro-sensitive translational stages

3. FINDINGS

Figure-3 shows the angles calculated with respect to the valve reference point at 8 different performance levels.

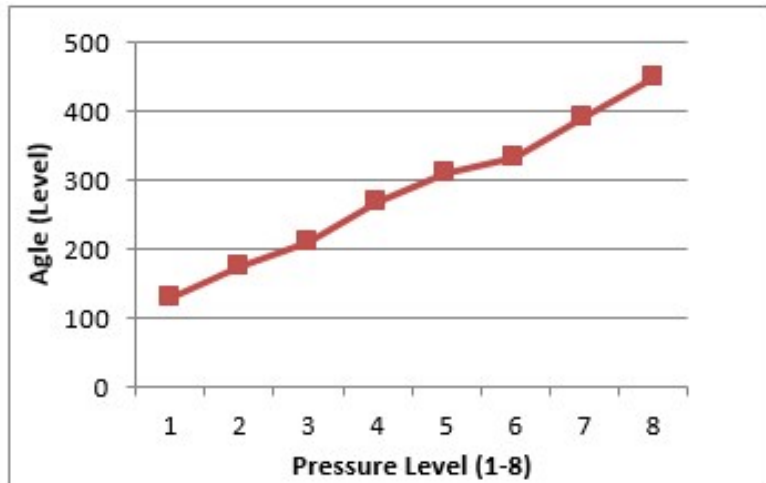


Figure 3. The angles calculated from the camera images according to the valve pressure level

The linear relationship between the angle and the pressure obtained by analyzing the camera images was found as,

$$\theta = 1,3314P + 106,22 \quad (1)$$

, where θ is the angle between the magnet and the reference point; and P is the valve opening pressure. Later, the valve was exposed to 30G and 90G magnetic fields at the 4th performance level (110 mmH₂O) and the 5th performance level (145 mmH₂O) to examine the effect of the permanent magnet on the valve. Immediately after the valve was exposed to the magnetic field, the images were captured by the camera and the change of the magnet angle with respect to the reference point was recorded. The angles measured at the fourth performance level of the valve and at 0 G, 30 G and 90 G magnetic fields are shown in Figure-4. Figure-5 describes how the angle for the fifth performance level changes over 30 G and 90 G magnetic fields.

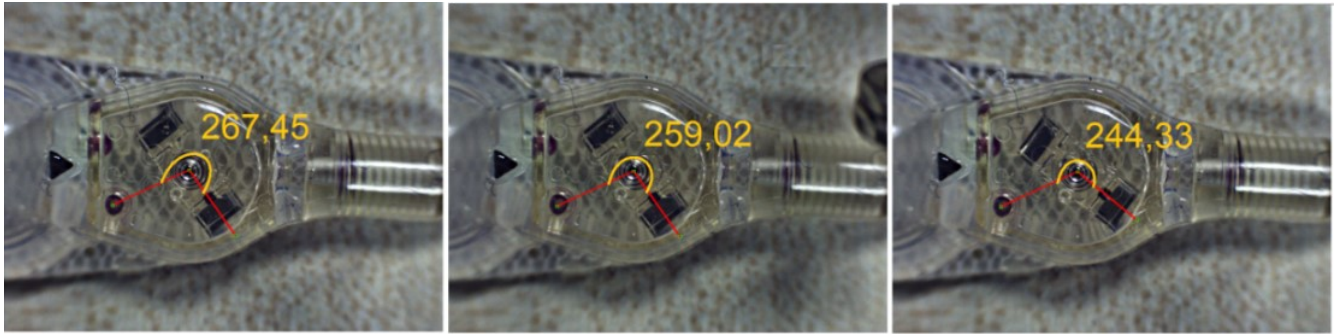


Figure 4. (110mmH₂O) a) 0G b) 30G c) 90 G the magnetic field effects at the fourth performance level

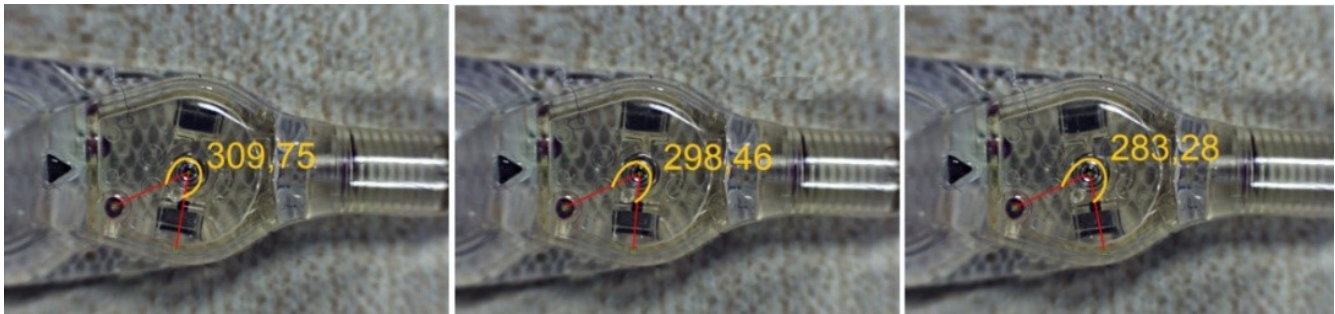


Figure 5. (145mmH₂O) a) 0G b) 30G c) 90 G the magnetic field effects at the fifth performance level

Comparisons were made with a low level of the tested performance level to determine whether the angle changes would change the valve performance level. '3rd Level Opening Pressure' and '4th Level Opening Pressure' are shown together in Figure-6. The graph contains \mp tolerances according to the tolerance percentages obtained from the valve datasheet. The angle alterations that occurred when the valve exposed to the 30G and 90G magnetic field are converted to pressure information according to the linear curve function (equation (1)) and added on the same graph. Although the opening pressure value has decreased, it has not reached the performance level of the previous level as it is seen in Figure-6.

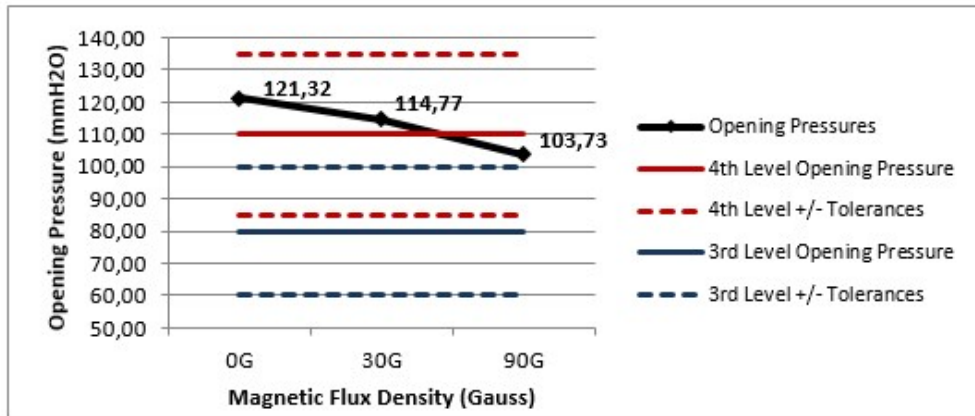


Figure 6. Comparison of the opening pressures of the third and fourth performance levels

'4th Level Opening Pressure' and '5th Level Opening Pressure' are shown together in Figure-7. The graph contains \mp tolerances according to the tolerance percentages obtained from the valve datasheet. The angle variations that occurred when the valve exposed to the 30G and 90G magnetic field are converted to pressure information according to the linear curve function (equation (1)) and added on the same graph. Although the angle level has decreased, it has not reached the distance of 4th performance level when the 30G magnetic field is applied at the 5th performance level as it is seen in Figure-7. However, when the 90G magnetic field is applied, the 4th performance level appears within the \mp tolerance distance.

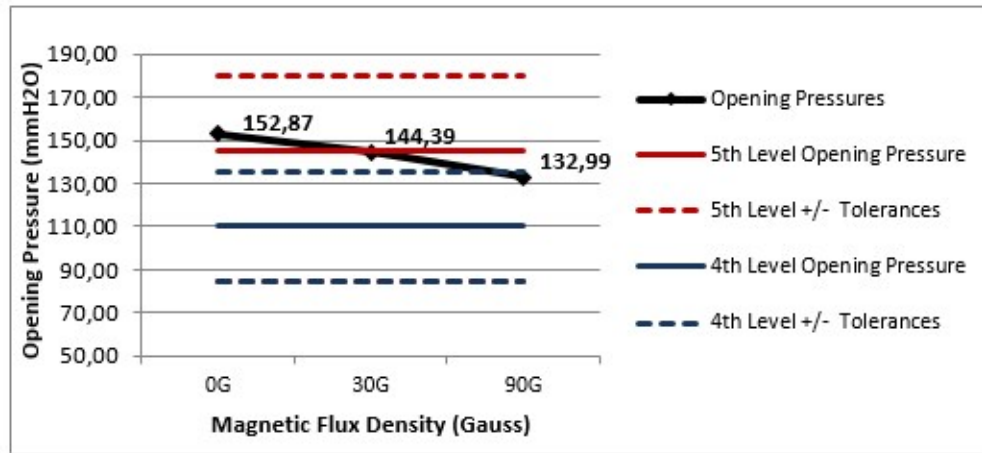


Figure 7. Comparison of the opening pressures of the fourth and fifth performance levels

*The 5th level -deviation is not seen because of the -deviation of the 5th level and 4th level pressure overlap at the 110 mmH₂O level

3.1 Magnetic flux density measurement of the headphones

The magnetic flux densities on the surface of the Apple EarPods headphone are depicted in Figure-8. As represented, the magnetic flux density reaches to a maximum of 169 G in the center of the headphone.

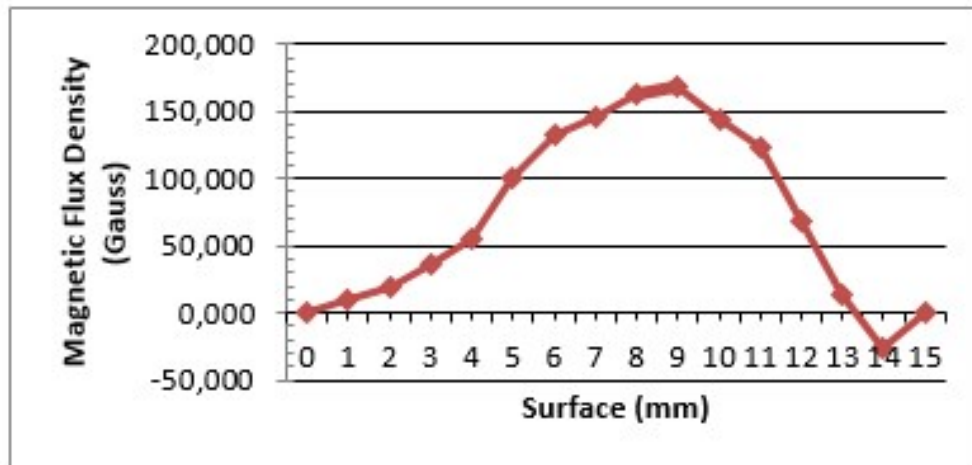


Figure 8. The magnetic flux density on the inner surface of the Apple headphone

The magnetic flux densities on the Philips SHE1350 headphone surface are delineated in Figure-9. As shown, the magnetic flux density reaches up to 231,4 G in the center of the headphone.

Table 1. Maximum magnetic flux densities (M.F.D.) as a function of distance from the headphone surfaces

	Max M.F.D. (G)							
	(0mm)	(1mm)	(2mm)	(3mm)	(4mm)	(5mm)	(6mm)	(7mm)
Apple Headphone	169,30	120,33	68,06	45,20	35,40	28,80	19,06	15,80
Philips Headphone	231,40	166,06	94,20	58,26	45,20	35,40	22,30	19,66

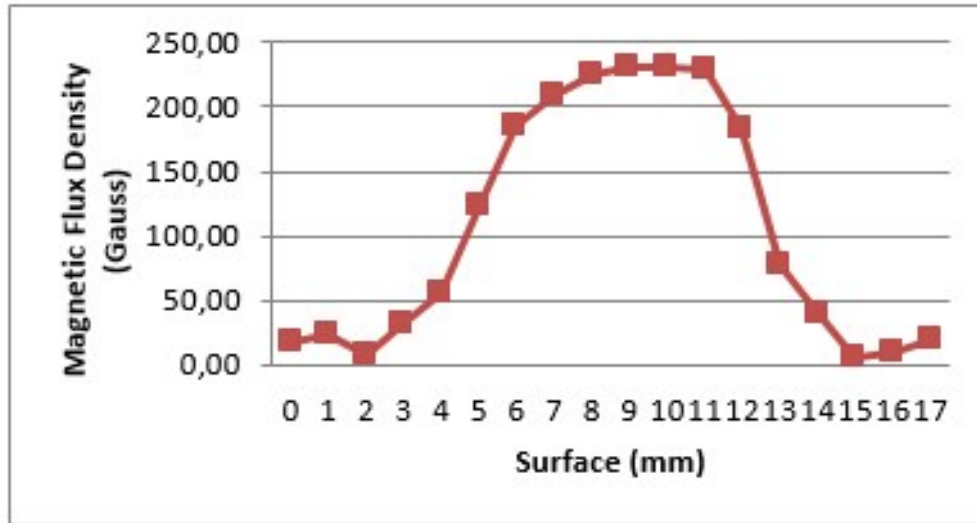


Figure 9. Magnetic flux density on the inner surface of the Philips headphone

In order to observe how the magnetic flux density changes when moving away from the headphones, the measurements were carried out by moving the sensor from the surface with 1 mm steps. The maximum flux densities measured for the two headphones as a function of the distance from the surface are listed in Table-1.

3.2 iPhone 6 Plus smartphone magnetic flux density measurement

The colormaps generated by magnetic flux densities measured laterally in increments of 0.5 mm from the surface on the reverse side of the loudspeaker part of the mobile phone are shown in Figure-10. The maximum flux density reaches up to 140 G at the nearest distance (1 mm) to the phone surface. Measured at 8 mm distance, this value decreases to 17 G. The maximum flux density is due to the phone’s built-in speaker with a permanent magnet. In addition, a zoom lens containing another permanent magnet on the camera side of the mobile phone also causes high magnetic flux density.

Table 2. Maximum magnetic flux densities as a function of distance away from four different regions of the mobile phone

	Distance from the surfaces of the regions (mm)							
	1	2	3	4	5	6	7	8
	Maximum Magnetic Flux Densities (G)							
Loudspeaker Part Front Side	218,33	162,80	126,86	90,93	68,06	55,00	45,20	41,93
Loudspeaker Part Reverse Side	141,00	108,33	78,93	59,33	49,53	39,73	36,46	33,20
Camera Part Reverse Side	114,86	82,20	59,33	65,86	39,73	39,73	39,73	36,46
Camera Part Front Side	58,26	41,93	35,40	25,60	22,33	15,80	15,80	12,53

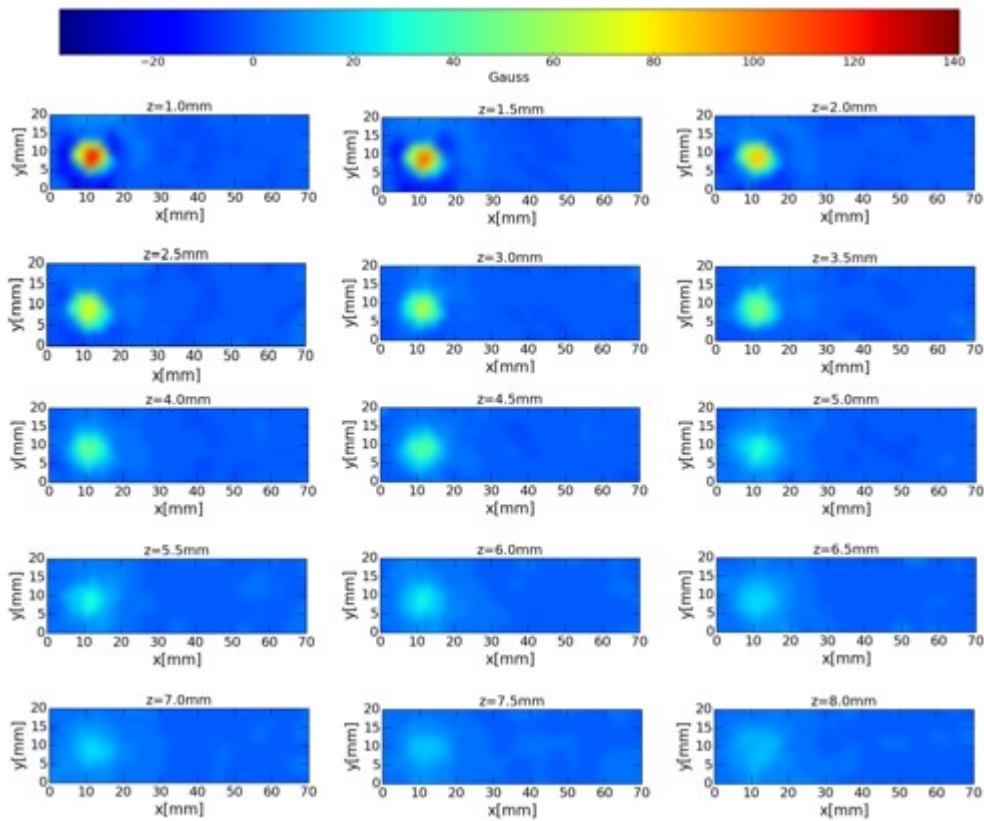


Figure 10. The magnetic maps of iPhone 6 Plus loudspeaker part at different distances on the reverse side

Scanning measurements have also been performed at the front side of the loudspeaker part, the reverse side of the camera part and the front side of the camera part. After generating the magnetic colormaps for all regions, it has also been investigated how the maximum magnetic flux density changes as a function of the distance from the surfaces of the regions. Table-2 shows the maximum magnetic flux densities obtained at different distances (from 1 mm to 8 mm) for four regions of the phone. The magnetic field is more than 90 G at 4 mm from the loudspeaker at the front of the mobile phone and over 40 G at 8 mm distance.

4. DISCUSSION

Table 3. Reported magnetic flux densities affecting different types of shunt valves [14]

Valve	Magnetic Flux Density (G)
Hakim	175
Sophy	400
Strata	60

4.1 The effect of magnetic field on the programmable shunt valves

The positional changes to the performance level of the magnets in the shunt valves were investigated in order to examine the effects of environmental magnetic fields on the programmable shunt valves. The angles corresponding to the performance levels were determined by calculating the angles of the magnet positions with respect to a reference point, and a linear relationship between the angle and the valve opening pressure was obtained. Thus, the position change caused by the effect of the magnetic flux density was expressed in terms of opening pressure change. The valve was exposed to 30 G and 90 G magnetic field at the 4th and 5th performance levels for the determination of these pressure changes. It was observed that as the magnetic field increases at the fourth performance level, the position of the valve magnet approaches to the third performance level. For this reason, the changes in the valve opening pressure were shown on a graph with the effect of the magnetic field applied to the 4th performance levels. As delineated in Figure-5, the opening pressures on the influence of the magnetic fields applied at the 4th performance level did not exceed the upper and lower limits of the 4th performance level and approached to the upper limit of the 3rd performance level but did not reach the tolerance range of this level. As the magnetic field was increased at the 5th performance level, it appeared that the valve magnet position approaches to the 4th performance level. For this reason, the valve opening pressure changes with the magnetic field effect applied at the 5th performance level were shown in Figure-6. Although the angle of the magnet under the 90 G magnetic field at 5th performance level did not exceed the lower limit of 5th performance level, it exceeded the upper limit of 4th performance level. In this case, it may be considered that the field of magnitude 90 G and above can lower the valve setting at the 5th performance level into the 4th performance level. This may cause that the valve set its opening pressure is set at 110mmH₂O instead of 145 mmH₂O, resulting in less BOS drainage. However, it is not possible to say that the performance level setting of this valve has been completely modified since the 5th performance level did not exceed the tolerance range.

4.2 The effect of headphones on the shunt valves

The headphones are closer to the shunt valve than the mobile phone because they are inserted into the inner ear. The maximum magnetic flux density measured for Apple and Philips headphones were 169.3 G and 231.4 G, respectively. Such magnetic flux densities produced by headphones are too high, and cannot be underestimated. Considering the effect of the relatively low magnetic field (90 G) on the opening pressure, the magnetic field, which is almost twice the magnitude, may cause serious changes in the opening pressure levels of the valves. For this reason, programmable shunt patients should be aware of the use of high-field-producing headphones.

4.3 The effect of iPhone smartphone on the shunt valves

Smartphones have four specific regions that create the high magnetic flux density: the camera, headphone, microphone, and the powerful speaker of the phone. The maximum magnetic flux density of 218 G was observed in the speaker region. The magnetic field generated by the mobile phone does not make a difference in the pressure setting as long as the phone is not in the close proximity of the shunt valve. However, the magnetic flux density at very close distances (2 mm and less) from the phone surface may still be above 90 G and may change the pressure setting.

Nomura et al. [14] analyzed the effect of mobile phones on 3 different valves which are not protected by 3T magnetic field. They have reported that the density at which the Strata valve was affected was 60 G, the Hakim valve was 175 G, and the Sophy valve was 400 G (Table-3). Strata is the most preferred valve brand in the world by physicians. The distance between the valve and the mobile phones should be particularly important for these valves, since the magnetic flux density of 60 G can be observed at a distance of 4-5 mm from the iPhone surface. In addition, as technology improves, parts such as zoom lenses and stronger permanent magnet speakers are used to get better sound and better quality images on smartphones. For this reason, it is expected that future devices will produce higher magnetic flux densities.

5. CONCLUSION

In this study, the effects of magnetic fields generated by devices such as headphones and mobile phones, which became part of everyday life, on programmable shunt valves were investigated. The experiments were performed on transparent shunts which allow optical inspection of valve settings in visible spectrum. However, comparable effects are also expected in opaque shunts as the pressure adjustment mechanism of almost all shunt types on the market is similar. As the results suggested, magnetic

fields produced by mobile phones and headphones may cause changes in pressure levels although some valve manufacturers claim that the valve opening pressure will not change even at 3 Tesla MR imaging.

Due to the cost of a new generation of 3T MR compatible shunt valves, earlier types of shunt valves (more susceptible to magnetic fields) are used in many countries, including Turkey. Therefore, it should be kept in mind that some devices have reversible effects without creating any radiological evidence on the programmable shunts, and any surgeon implanting these valves and any patient carrying them should be aware of the possible effects. Patients with severe hydrocephalus can replace devices that produce critical magnetic fields with devices that emit fewer magnetic fields to reduce such potential hazards. Also, if patients use non-implanted side of their heads to respond to phone calls, the magnetic field in the shunt valve will fall to an ineffective level as the distance between the shunt valve and the phone increases.

References

- [1] A. Aschoff, P. Kremer, B. Hashemi, and S. Kunze, “The scientific history of hydrocephalus and its treatment,” *Neurosurgical review*, vol. 22, no. 2-3, pp. 67–93, 1999.
- [2] R. C. Anderson, M. L. Walker, J. M. Viner, and J. R. Kestle, “Adjustment and malfunction of a programmable valve after exposure to toy magnets: case report,” *Journal of Neurosurgery: Pediatrics*, vol. 101, no. 2, pp. 222–225, 2004.
- [3] S. Utsuki, S. Shimizu, H. Oka, S. Suzuki, and K. Fujii, “Alteration of the pressure setting of a codman-hakim programmable valve by a television,” *Neurologia medico-chirurgica*, vol. 46, no. 8, pp. 405–407, 2006.
- [4] M. R. Guilfoyle, H. Fernandes, and S. Price, “In vivo alteration of strata valve setting by vagus nerve stimulator-activating magnet,” *British journal of neurosurgery*, vol. 21, no. 1, pp. 41–42, 2007.
- [5] S. Ozturk, H. Cakin, H. Kurtuldu, O. Kocak, F. S. Erol, and M. Kaplan, “Smartphones and programmable shunts: Are these indispensable phones safe and smart?” *World neurosurgery*, vol. 102, pp. 518–525, 2017.
- [6] A. Lavinio, S. Harding, F. Van Der Boogaard, M. Czosnyka, P. Smielewski, H. K. Richards, J. D. Pickard, and Z. H. Czosnyka, “Magnetic field interactions in adjustable hydrocephalus shunts,” 2008.
- [7] H. S. Spader, L. Ratanaprasatporn, J. F. Morrison, J. A. Grossberg, and G. R. Cosgrove, “Programmable shunts and headphones: Are they safe together?” *Journal of Neurosurgery: Pediatrics*, vol. 16, no. 4, pp. 402–405, 2015.
- [8] I. AltuN, K. Z. YUKSEL, and T. Mert, “Impact of magnetic field on pressures of programmable cerebrospinal fluid shunts: An experimental study,” *Turkish neurosurgery*, vol. 27, no. 6, 2016.
- [9] M. Lefranc, J. Y. L. Ko, J. Peltier, A. Fichten, C. Desenclos, J.-M. Macron, P. Toussaint, D. Le Gars, and M. Petitjean, “Effect of transcranial magnetic stimulation on four types of pressure-programmable valves,” *Acta neurochirurgica*, vol. 152, no. 4, pp. 689–697, 2010.
- [10] Y. He, R. K. Murphy, J. L. Roland, and D. D. Limbrick, “Interactions between programmable shunt valves and the ipad 3 with smart cover,” *Child’s Nervous System*, vol. 29, no. 4, pp. 531–533, 2013.
- [11] T. J. Zuzak, B. Balmer, D. Schmidig, E. Boltshauser, and M. A. Grotzer, “Magnetic toys: forbidden for pediatric patients with certain programmable shunt valves?” *Child’s Nervous System*, vol. 25, no. 2, p. 161, 2009.
- [12] F. G. Shellock, S. F. Wilson, and C. P. Mauge, “Magnetically programmable shunt valve: Mri at 3-tesla,” *Magnetic resonance imaging*, vol. 25, no. 7, pp. 1116–1121, 2007.
- [13] T. Inoue, Y. Kuzu, K. Ogasawara, and A. Ogawa, “Effect of 3-tesla magnetic resonance imaging on various pressure programmable shunt valves,” *Journal of Neurosurgery: Pediatrics*, vol. 103, no. 2, pp. 163–165, 2005.
- [14] S. Nomura, H. Fujisawa, and M. Suzuki, “Effect of cell phone magnetic fields on adjustable cerebrospinal fluid shunt valves,” *Surgical neurology*, vol. 63, no. 5, pp. 467–468, 2005.

Bioremediation of wastewaters from local textile industries

Abdullahi Ajao ^{*1} , Sunday Awe 

Abstract

The present study evaluates the bioremediation potential of indigenous bacterial species isolated from dye-contaminated soil samples from small dyeing outlet located in Ilorin. The water pollution index was estimated based on the physicochemical characteristics and heavy metal concentrations of the raw (Day 0) and treated textile wastewater such as pH, biochemical oxygen demand-5, chemical oxygen demand, total suspended solids and total dissolved solid with mean values of 8.85 ± 0.45 mg/L, 1200 ± 21.3 mg/L, 2440 ± 31.3 mg/L, 1660 ± 17.2 mg/L and 2650 ± 28.1 mg/L respectively, similarly, Lead was the most abundant heavy metal detected in the sample while Cadmium concentration was the lowest with the mean values of 3.52 ± 0.00 mg/L and 2.18 ± 0.00 mg/L respectively. The bacterial strain with highest dye decolorization capacity was screened and identified as *Bacillus licheniformis* ZUL012. The isolate was consequently used for the bioremediation of the wastewater over a period of 10 days. The results showed an incredible reduction in the physicochemical characteristics and heavy metal concentrations of the textile wastewater in the following ranges (8.85-6.55), (1200-300) mg/L, (2440-518) mg/L, (1660-666) mg/L and (2650-920) mg/L with the highest removal efficiency of 75 %, 78 %, 60 %, 65 %, recorded for biochemical oxygen demand, chemical oxygen demand, total suspended solid, total dissolved solid, respectively while that of heavy metals such as lead, cadmium, chromium and nickel were 80 %, 60 %, 67 %, 72 % reduction, respectively. Laccase and Azoreductase activities tend to decrease as the pH gradually moved towards acidic condition during the bioremediation process. Toxicity of the treated effluent was assessed using Maize and Bean seed germination test. Conclusively, these research findings can serve as a framework for the outlet design of wastewater treatment plant for local textile outlets.

Keywords

Bacillus; Bioremediation; Enzymes; Fourier transformed infrared spectroscopy (FTIR); Gas chromatography-mass spectrometry (GC-MS); Physicochemicals; Textile wastewater.

¹ Kwara State University

*Corresponding Author: abdullahi.ajao@kwasu.edu.ng

Manuscript received date: December 18, 2018

Accept Date: December 31, 2018

Published Date: December 31, 2018.

1. INTRODUCTION

Textile industries consume several million tons of synthetic dyes (around 56%) of world total annual production (Adegoke and Bello, 2015; Markandeya et al., 2017). A large volume of water is needed during the operations in the textile industry thereby, generating a tremendous amount of wastewater containing a significant amount of unfixed dyes (Markadeya et al., 2017). Apparently, the indiscriminate discharge of such toxic wastewaters in and around the residential and industrial areas constitute major environmental and health hazard. Several illnesses, tumors, cancers, and various allergies have been linked to the Azo dyes content in textile wastewaters that are found to be toxic, mutagenic and recalcitrance in nature (Shah, 2018; Yaseen and Scholz, 2018) The complex aromatic structure of these dyes makes it recalcitrant to degradation and conventional treatment methods are found to be ineffective (Adegoke and Bello, 2015). The available strategies for the dyes containing wastewater treatment have been the physicochemical methods (Das et al., 2016; Shah, 2018). However, application of each of these strategies has been characterized with numerous shortcomings including large usage of chemical or sludge deposition with apparent disposal issues; expensive operating and plant requirement, ineffective in color reduction especially Azo dyes (Fayidh et al., 2011). Bioremediation is the application of microorganisms in the waste management system, which exploits

microorganisms for the removal and recycling of pollutants in the environment (Endeshaw et al., 2017). Microorganisms with diverse catabolic versatility utilize organic pollutants as their energy source and break down those pollutants into non-toxic intermediate compounds. Bioremediation strategy is receiving more attention due to its cost-effectiveness, and diverse metabolic versatility of microorganisms involved (Pandey et al., 2007). The survival and adaptability of organisms in dye contaminated sites make them incredibly tolerant to the toxic effect of high dye concentrations; therefore can be used effectively for the bioremediation of colored effluent released from various fabric processing units (Ogugbue et al., 2012). Application of this approach on an industrial scale becomes difficult due to the complexity of dye constituents of textile wastewater. However, a continued search for the new organisms and technologies are required to make this process of bioremediation more industrially viable, cheap and ecofriendly remediation technology. Consequently, the present study was carried to investigate the bioremediation potential of indigenous bacteria towards bioremediation of local textile wastewater obtained from the local outlet. This study was undertaken in the Department of Microbiology, Kwara State University, Malete, Nigeria in 2017-2018.

2. Materials & Methods

Sample collection

The Local textile wastewater and soil contaminated with dye effluents were collected from small dyeing outlet situated within Ilorin metropolis, Kwara State, Nigeria in sterile screw-capped plastic containers, then transported to the Microbiology Laboratory, Malete for the experiment.

Characterization of local textile wastewaters

The Pollution load assessment of the local textile wastewater was investigated using physicochemical parameters and heavy metal concentrations namely Chemical Oxygen Demand (COD) Biological Oxygen Demand, Total Suspended Solid, Total Dissolved Solid and pH. Also, heavy metal concentrations such as Lead, Cadmium, Chromium, and Nickel were determined following standard methods (APHA, 1999). These parameters served as a measure of the pollution index, performance criteria and efficiency of the bioremediation process. The heavy metal pollution levels were analyzed using atomic adsorption spectrophotometer (AAS -model-GBC-932 plus Chem Tech-USA)

Enrichment techniques and isolation of potential dye degrading bacteria

Textile wastewater sample was enriched using a modified method of Olukanni et al. (2013). Aliquot of 5 mL soil suspension obtained from 10 g of dye polluted soil samples suspended in 100 ml of sterile distilled water was added to the nutrient broth containing 10% of the sterilized textile effluents in 250 ml Erlenmeyer flasks, then kept at 30 °C for 48 hours in an orbital shaker at 150 rpm. One milliliter of the enriched bacterial culture was picked and serially diluted and inoculated on the nutrient agar plates. After 48 hr of incubation, the morphologically distinct bacterial colonies further purified by repeated streaking on nutrient agar plates. The bacterial colony with high growth rate and decolorization potential was selected and identified based on the Gram reaction and biochemical test, then stored below 10 °C on nutrient agar slopes for molecular Identification

16SrDNA sequences processing

Genomic DNA of the isolate was extracted following standard method. PCR amplification was carried out as follows: A pair of universal primer of 27F (5-AGAGTTTGTATCCTGGCTCAG-3) and 1492R (5- GGTTACCTTGTTACGACTT-3) was added to 2.5 μl PCR buffer containing 2 μl dNTP mix, 0.2 μl Taq DNA polymerase, 5 μl of DNA template and 12.8 μl sterile distilled water made up 25 μl reaction volumes. The thermo-cycler PCR conditions were as follows: denaturation (92 °C/1 min), annealing (54 °C/ 1 min) and extension (72 °C / 1 min) in 30 cycles (Miller et al., 2013). PCR product was loaded into well and electrophoresed on agarose gel at 120V for 45 minutes using a maxi gel system. The band on the gels was visualized by ultraviolet trans-illumination (Uvitec, Cambridge, UK), then sequenced. The 16S rRNA sequences of the isolate and similar sequences downloaded from NCBI database using the BLAST search program were aligned using the multiple sequence alignment and dendrogram was generated using MEGA 6.0.

Bioremediation process

The dye degrading cell was grown in nutrient broth and incubated for 8 hours to attain exponential growth phase at the optical density (OD_{600 nm}=1.0 which correspond to 10⁹ cfu/ml were used as inoculums. Fifty milliliters of the textile wastewater was added to the 150 ml of nutrient broth in a 250 ml Erlenmeyer flask and sterilized in an autoclave at 121 °C for 15 minutes. It was allowed to cool, then inoculated with 20 ml of the inoculums, incubated at 30 °C on a rotary shaker at 120 rpm for 10 days. Six different setups were made. Physicochemical parameters, enzymatic activities, Extracellular proteins, and Total viable counts were determined at 48-hour intervals from the experimental flasks over a period of 10 days to monitor the progress of the treatment. Fourier transformed infrared spectroscopy (FTIR); Gas chromatography-mass spectrometry (GC-MS) was used for the confirmation of the biodegradation process

Fourier transformed infrared spectroscopy (FTIR) analysis

The experimental setup of both the control and treated samples were investigated to assess the functional groups in both samples. The samples were centrifuged at 4000rpm for 20 min. The residual dyes in the wastewater were extracted with Ethyl acetate, One μl of sample was run in FTIR using KBr pellets, JASCO FT/IR 4100 generated an infrared spectral at 400-4000/cm scanning range.

Gas chromatography-mass spectroscopy

The number and the chemical constituents of both treated and control local textile wastewater were determined using the Gas chromatography-mass spectroscopy (GC-MS). A 10-day treated wastewater and control samples were centrifuged at $8,944 \times g$ for 10 min and then extracted with ethyl acetate in a separating funnel, dried in a rotary evaporator and re-dissolved in high analytical grade methanol for GC-MS analyses.

Enzymatic assay and growth patterns

Enzyme Assay was carried out to determine the expression of Laccase and Azoreductase activities in the experimental flasks during the bioremediation process. The spectrophotometric method of Collins and Dobson (1997) was adopted for the determination of laccase activities while; Azoreductase activity was determined using the method of Leelakriangsak and Borisut, (2012). Bradford's method was used for the estimation of protein Content as described by Singh and Abraham (2013). Total Viable counts were estimated carrying out serial dilution method and pour plate method (Fawole and Oso, 2001).

Seed germination assay

The toxicity of both treated and control samples was investigated using seed germination test, this test measured the impact of the textile wastewater on the crops as well as to assert the possible reuse of the treated wastewater for the irrigation of agricultural fields after bioremediation. The experiment was carried out in Petri dishes whose top and bottom was padded with a layer of tissue paper as follows; Each of the padded Petri dishes contained 20 seeds each of maize and beans separately which were soaked with 25 ml of treated and distilled water used as the control. The set-up was incubated for 7 days for germination to occur. The percentage of seed germination was calculated using Eq. 1.

$$\text{Germination}(\%) = \frac{\text{Number of seeds germinated} \times 100}{\text{Total number of seeds}} \quad (1)$$

Data entry and analysis

The means values of the physicochemical parameters and heavy metal concentration of the textile wastewater samples were shown in Tables. The mean values of the data obtained during growth patterns and enzymatic activities were analyzed using One-way ANOVA, where there were differences between the means, post hoc test was carried out using Duncan multiple range tests to rank the mean values. Level of significance was set at $p \leq 0.05$.

Table 1. Bioremediation of textile wastewater by *Bacillus licheniformis* ZUL012

Parameter	Period of degradation (Days)						Efficiency (%)
	0?	2	4	6	8	10	
pH	8.85±0.45	7.80±0.10	8.00±0.00	7.20±0.45	6.85±0.00	6.55±0.34	NA
BOD5 (mg/L)	1200.0±21.3	950.0±6.7	820.0±8.8	768.0±5.3	552.0±5.9	300.00±15.6	75
COD (mg/L)	2440.0±31.3	1450.0±11.0	1260.0±16.1	983.0±12.4	718.0±9.0	518.0±7.6	78
TSS (mg/L)	1660.0±17.2	1550.0±18.2	1360.0±12.7	1120.0±10.2	892.0±8.2	666.0±12.9	60
TDS (mg/L)	2650.0±28.1	2160.0±30.7	1786.0±21.9	1442.0±14.1	1176.0±12.5	920.0±13.1	65
Pb (mg/L)	3.12±0.55	3.00±0.00	2.87±0.00	2.02±0.00	1.92±0.00	1.88±0.00	80
Cd (mg/L)	2.18±0.00	2.04±0.03	1.96±0.00	1.58±0.00	1.20±0.02	0.86±0.03	60
Cr (mg/L)	3.20±0.23	3.06±0.00	2.64±0.04	2.10±0.05	1.67±0.00	1.06±0.00	67
Ni (mg/L)	3.52±0.00	3.11±0.08	2.74±0.07	2.03±0.00	1.76±0.06	1.00±0.00	72
pH= Potential of Hydrogen; BOD = Biological Oxygen Demand; TSS = Total Suspended Solids; NA=Not Applicable							
TDS = Total Dissolved Solids; COD = Chemical Oxygen Demand. (Mean±SEM); N=3; Day 0 = Non-Treated sample							

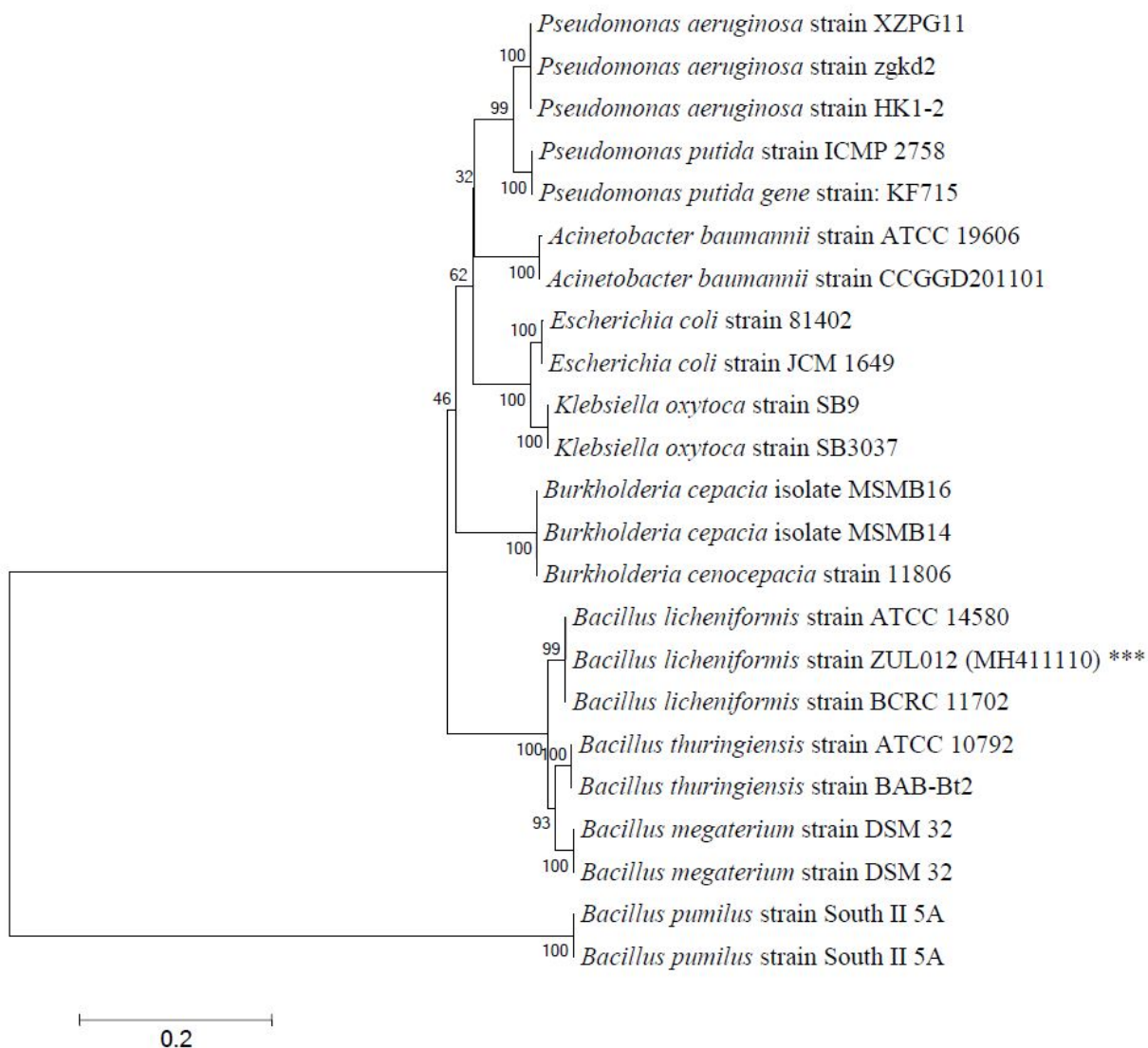


Figure 1. Constructed Phylogenetic tree of the partial 16S rDNA sequences using Neighbor-Joining method. The scale bar corresponds to 0.2 changes per nucleotide. Numbers in parenthesis and asteriks represent GenBank accession numbers.

Table 2. Growth Patterns and Enzymatic Activities during Bioremediation of Local Textile wastewater by *Bacillus licheniformis* ZUL012

Parameter	Period of degradation (Days)				
	2	4	6	8	10
pH	8.65±1.15a	8.00±0.81a	7.12±0.05a	7.65±1.15b	6.55±0.31c
Extracellular protein (mg)	12.60.0±1.42b	17.86±2.49a	14.26±1.33ab	11.55±1.62b	7.425±0.00c
Laccase activities (U/mg)	1.821±0.10a	1.726±0.22a	0.735±0.00b	0.551±0.11c	0.346±0.00d
Azo-reductase activities (U/mg)	2.00±0.12a	2.107±0.21a	1.980±0.00ab	1.426±0.32b	1.130±0.00bc
TVC (Log cfu/ml)	3.65	4.75	6.41	5.54	5.94

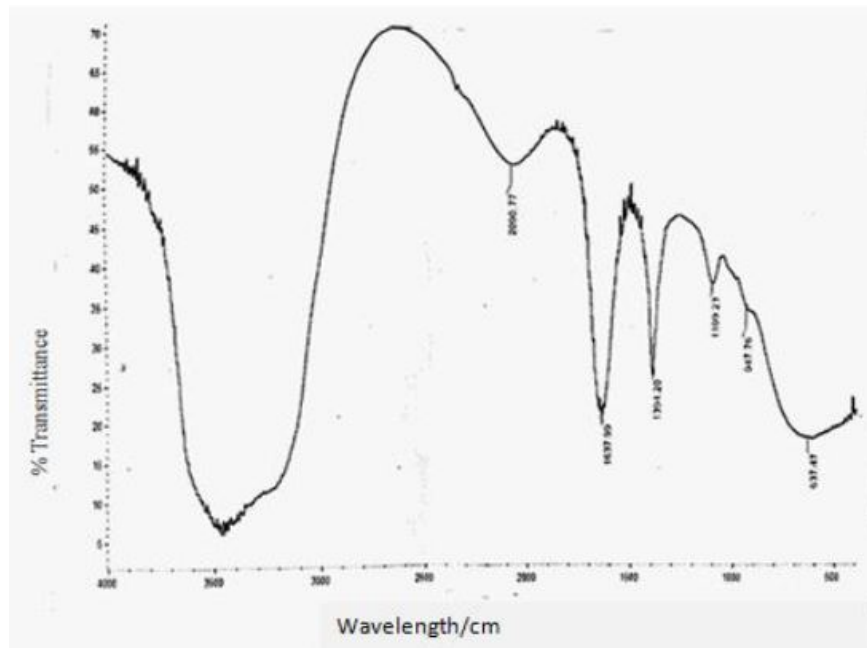


Figure 2. FTIR spectra of local textile wastewater (Control)

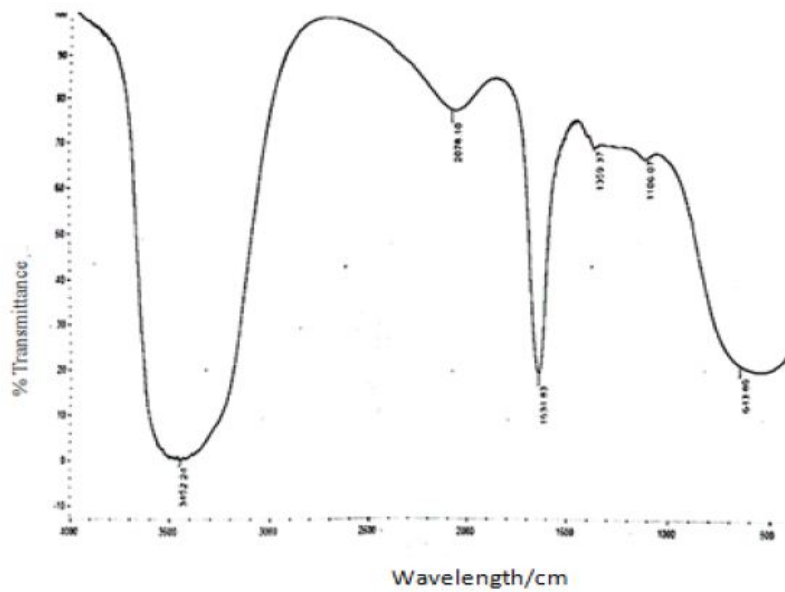


Figure 3. FTIR spectra of local textile wastewater Treated with *Bacillus licheniformis* Zul 012

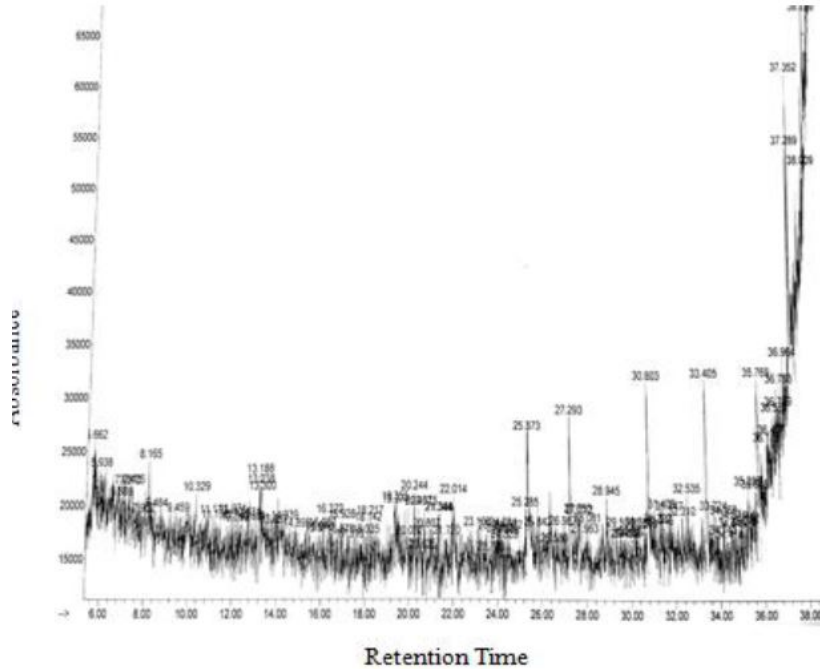


Figure 4. Chromatogram analysis of local textile wastewater (control)

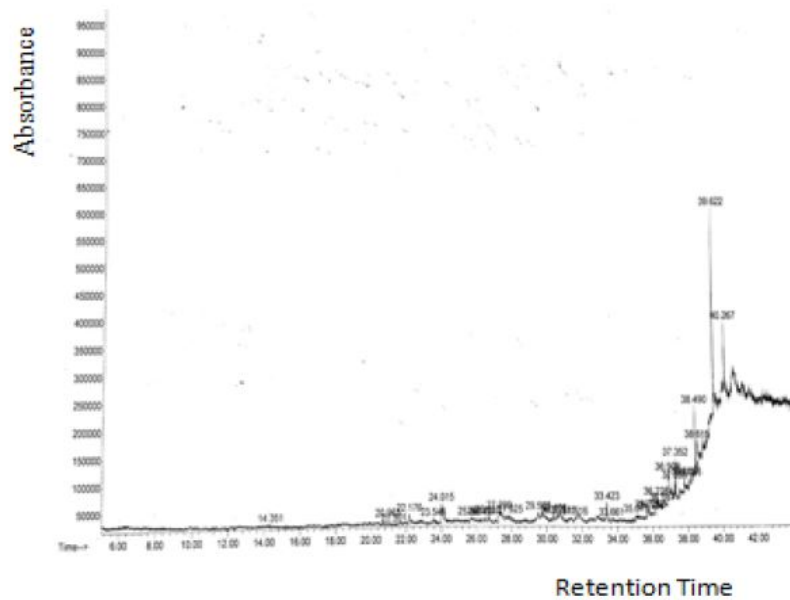


Figure 5. Chromatogram analysis of Local Textile wastewater Treated with *Bacillus licheniformis* ZUL012

3. Results

The wastewater from the local textile outlets was characterized by its following parameters; pH, BOD₅, COD, TDS and TSS Likewise heavy metal concentrations. The mean values of the parameters of both untreated (raw) and the treated wastewater are shown in Table 1. The values of the parameters obtained are designated as Day 0. While the values recorded at 2- day interval for a 10-day treatment are presented as period of degradation (2-10 days). High values recorded for all the parameters underscored its degree of contamination and pollution load index. (Table 1) The initial pH of the sample at day 0 was found to be slightly alkaline with pH of 8.85. Similarly, the total dissolved solids and total suspended solids recorded were 2650 mg/L and 1660 mg/L respectively, above the discharge limit of 787 mg/L and 574 mg/L (APHA, 2005), which can be attributed to the presence of synthetic dyes and other chemical constituents of the wastewater samples (Mohabansi et al., 2011). Similar results of high TDS in textile effluents had been reported by Paul et al. (2012). The COD and BOD levels were higher than the

permissible limit; this underlined the oxygen-depletion properties of the wastewater. The heavy metal concentrations were recorded in the following ranges: Cadmium (2.18 mg/L), Lead (3.12 mg/L), Chromium (3.20 mg/L) and Nickel (3.52 mg/L). This was in the same order of magnitude as reported by Naeem et al. (2009). The major sources of heavy metals in textile wastewater include types of dyestuff, chemicals and even the water used during different stages of textile production as such heavy metal toxicity may affect soil fertility, microbial population size, diversity and activity (Ayansina and Olubukola, 2017). Especially when released into the environment without proper treatment.

The overall findings of the physicochemical characteristics and heavy metal ion concentrations of the textile wastewater demonstrated the high pollution index of the wastewater which in line with what was obtained in the similar study both in Nigeria and India (Awomeso et al., 2010; Vigneshpriya and Shanthi, 2015). *Bacillus licheniformis* strain Zul012 isolated in this study was explored for the bioremediation process. The isolate showed significant reduction in all the selected physicochemical characteristics and metal ion concentrations (Table 1). The initial pH of the sample before treatment was 8.85 which were changed to slightly acidic with the mean pH values of 6.55. *B. licheniformis* strain Zul012 showed remarkable reduction in BOD₅ (1200-300) mg/L, COD (2440-518) mg/L, TSS (1660-666) mg/L and TDS (2650-920) mg/L with the highest removal efficiency of 75 %, 78 %, 60 % and 65 % respectively after 10 days of treatment. Many studies have validated the successful applications of different *Bacillus* spp for the bioremediation of textile effluents (Kayode-Isola et al. 2008; Prasad et al. 2010; Usman et al. 2012; Ogunjobi et al. 2012). Apparently, *Bacillus* spp have proven to poses metabolic and enzymatic capacity to degrade textile wastes. The removal of TSS, TDS, COD and BOD observed in this study agreed with the findings of Prasad and Bhaskara (2010); Ajao et al. (2011) and Samuel et al. (2011). This remarkable reduction of all the contaminants observed after bioremediation agreed with the findings of Ranjamohan and Karthikayam (2004); Salisu and Mustapha (2010); Ajao et al. (2011) who reported high degree of reduction in BOD having 97%, TSS (85%), TDS and (96%) by *Bacillus megaterium*, *Pseudomonas aeruginosa* and *Alcaligenes faecalis* to the regulatory acceptable limit. The current findings showed that *Bacillus licheniformis* ZUL012 demonstrated high biosorption capacity for some selected heavy metals in this order (Pb from 3.12 to 1.88 mg/L representing 80%, Cd from 2.18 to 0.86 mg/L representing 60%, Cr from 3.20 to 1.06 mg/L representing 67% and Ni from 3.52 to 1.00 mg/L representing 72%) similar to the work of Wang et al. (2010); Ajao et al., 2011; Mathiyazhagan et al. (2011) Though, there was a variance in the metal-adsorption capacity to specific metals observed in this current study. The phylogenetic tree of *Bacillus licheniformis* 16S rDNA sequences and related bacterial sequences was represented is shown in Fig. 1. Biodegradation efficiency of the isolate can be attributed to the adaptability and acclimatization of the *Bacillus licheniformis* to the dye contaminated soil. This isolate might have probably acquired natural adaptation or through horizontal gene transfer to surviving and acquired the genes involved in the degradation of dyes. *Bacillus* spp posses high decolorization potential and ability to recondition the physicochemical properties of the textile wastewater (Srinivasan et al., 2014). Nutrient broth supplemented with the textile wastewater used as biodegradation broth in this study contained beef extract, yeast extract and peptone that might have served as primary substrate in the co-metabolism of textile effluent, which might have accounted for the remarkable degradation efficiency of the *B. licheniformis* (Mahmood et al., 2015) achieved in this study. Some Authors had also reported that yeast extract, sucrose, maltose, and sodium carbonate are commonly added as co-substrate for efficient textile effluents decolorisation by bacterial species which may, therefore, be regarded as cometabolism (Moosvi et al., 2007; Saratale et al., 2009; Elisangela et al., 2009; Mahmood et al., 2015). The pH, extracellular protein content, laccase activities, azoreductase activities, and total viable counts were used as surrogate indicators for monitoring the performance and evidence of bioremediation process (Table 3). The laccase activities, extracellular protein and azoreductase activities were found to be pH dependent, as they tend to decrease as pH gradually moved towards acidic. This finding suggests that alkaline pH tends to favor the growth and enzyme production (Rajeswari and Bhuvaneshwari, 2016). However, since decolorization is not synonymous to detoxification, similarly, GC-MS and FTIR cannot be used to measure the toxicity of the end products, therefore, Assessment of the toxicity of the degradation products was evaluated (Bilal et al., 2016). Since the treated effluent will eventually be released into the river or soil, toxicity impact of those degradation products on the crops as a measure of treatment efficiency of the bioremediation process was determined (Saratale et al., 2009; Jadhav et al., 2010). Several infrared spectral detected both in the control and treated samples represent fingerprints with absorption peaks presented in Figs. 2 and 3 respectively. Six peaks were conspicuously observed from the spectra at the frequency region between 500-4000/cm with stretching type of vibrations at low and high peaks of the spectrum. Similarly, some functional groups were not detected in the treated textile wastewater. Peaks of the fingerprint region (500 to 1500/cm) indicate the mono-substituted and para-disubstituted benzene rings representing aromatic metabolites in the samples. The spectrum at a peak of 643.80 and 650/cm represent strong C-Br stretching, halo compound. A peak of 1106.07 and 1000/cm represent strong C-O stretching, secondary alcohol. A peak of 1359.37 and 1400/cm indicates strong S=O stretching, sulfonamide. While a peak of 1634.83 and 1600/cm connote strong C=C stretching monosubstituted alkene. A peak of 2078.10 at 2050/cm for strong N=C=S stretching isothiocyanate. A peak of 3452.24 and 3450/cm indicate strong O-H stretching intermolecular bonded alcohol was detected. However, some functional groups were not detected in the treated dye which can be attributed to the degradation of some metabolites present in the control samples. The chromatogram of both the control and treated textile effluent is shown in Fig. 4 and 5. The fragmentation patterns

and mass per charges (m/z) values obtained from GC chromatogram and mass spectra were used to assign the structures and nomenclature of the compounds detected both in the treated and control wastewater samples represented by peaks. Each peak represents a compound. A number of peaks in the control samples found to be higher than in the treated samples this validates the degradation of the compounds in the treated samples during bioremediation. However, degradation is not synonymous with detoxification; therefore, phytotoxicity assessment of both treated and control local wastewater samples indicated that the seed watered with non-treated textile samples showed a tremendous toxic effect on both maize and beans seed germination. In contrast, treated dyes reduced the toxic effect of the effluents on the seed germination rate.

4. Conclusion

The main outcome of this work is the isolation of novel bacterial strain from the soil contaminated with textile wastewater that can effectively degrade local textile wastewater. Isolated bacterial species showed high dye degradation potential. Therefore this study demonstrates the successful utilization of pure culture of *Bacillus licheniformis* ZUL012 for the decolorization of local textile wastewater. Interestingly, the evidence for bacterial bioremediation of effluent from textile wastewaters was established. The reduction in BOD, COD, TSS, TDS, and biosorption of metal ions in a varying magnitude are appreciable. The removal efficiency in the level of pollutants and heavy metal biosorption paved way for the adoption of this bacterial sp for the treatment of textile wastewater in large scale.

Acknowledgement

Authors express their gratitude to the Management of Kwara State University, Malete for providing necessary facilities for the successful completion of this work.




References

- Adegoke, K.; Bello, O.S., (2015). Dye sequestering using agricultural wastes as adsorbents. *Water Resour. Ind.*, 12: 8-24.
- Ajao, A.T.; Adebayo, G.B.; Yakubu, S.E., (2011). Bioremediation of textile industrial effluent using mixed culture of *Pseudomonas aeruginosa* and *Bacillus subtilis* immobilized on agar agar in a Bioreactor. *J. Microbiol. Biotech. Res.*, 1(3): 50-56.
- APHA (2005) Standard Methods for the Examination of Water and Wastewater. 21st Edition, American Public Health Association/American Water Works Association/Water Environment Federation, Washington DC., USA.
- Awomeso, J.A.; Taiwo, A.M.; Gbadebo, A.M.; Adenowo, J.A., (2010). Studies on the pollution of waterbody by textile Industry effluents in Lagos, Nigeria. *J. Appl. Sci. Environ. Sanit*, 5: 353-359.
- Ayansina S. A.; Olubukola, O. B., (2017) Review A New Strategy for Heavy Metal Polluted Environments: A Review of Microbial Biosorbents. *Int. J. Environ. Res. Public Health*, 14: 94
- Bilal, M.; Iqbal, M.; Hu, H.; Zhang, X., (2016). Mutagenicity and cytotoxicity assessment of biodegraded textile effluent by Ca-alginate encapsulated manganese peroxidase. *Biochem. Eng. J.*, (3):1010-1016.
- Collins, P. J.; Dobson, A. D. W., (1997). Regulation of laccase gene transcription in *Trametes versicolor*. *Appl. Environ. Microbiol.*, 63: 3444-3450.
- Das, A.; Mishra, S., (2016). Decolorization of different textile azo dyes using an isolated *Enterococcus durranis* GM13. *Int. J. Curr. Microbiol. App. Sci.*, 5(7): 676-686.
- Elisangela, F.; Rea, Z.; Fabio, D.G.; Cristiano, R.M.; Regina, D.L., (2009). Biodegradation of textile azo dyes by a facultative *Staphylococcus arlettae* strain VN-11 using a sequential microaerophilic/aerobic process. *Int. Biodeter. Biodegr.*, 63:280-288.
- Endeshaw, A.; Birhanu, G.; Zerihun, T.; Misganaw, W., (2017) Application of microorganisms in bioremediation-review *J. Environ. Microb.*, 1(1): 2-9.
- Fawole, M.O.; Oso, B.A., (2001). *Laboratory Manual of Microbiology*. Revised Edition, Spectrum Books, Ibadan. Kaushik,

- G.; Thakur, I.S., (2014). Production of laccase and optimization of its production by *Bacillus* sp. using distillery spent wash as inducer. *Bioremediat. J.*, 18: 28-37.
- Kayode-Isola, T.M.; Eniola, K. I. T.; Olayemi A.B.; Igunnugbemi, O.O., (2008). Response of Resident Bacteria of a Crude Oil-Polluted River to Diesel Oil. *Amer- Eura. J. Agr.*, 1:06-09.
- Mahmood, S.; Khalid, A.; Mahmood, T.; Arshad, M.; Ahmad, R., (2015). Potential of newly isolated bacterial strains for simultaneous removal of hexavalent chromium and reactive black-5 azo dye from tannery effluent. *J. Chem. Technol. Biotechnol.*, 88(8): 1506-1513.
- Markandeya , T.; Shukla, S.P.; Mohan, D., (2017). Toxicity of Disperse Dyes and its Removal from Wastewater Using Various Adsorbents: A Review. *Res. J. Environ. Toxic.*, 11: 72-89.
- Mathiyazhagan, N.; Natarajan, D., (2011). Bioremediation of effluent from magnesite and bauxites and textile mine using *Thiobacillus* spp and *Pseudomonas* spp. *J. Bioremed. Biodegrad.*, 2:115. doi: 10.4172/2155-6199.1000115.
- Miller, C.S.; Handley, K.M.; Wrighton, K.C.; Frischkorn, K.R.; Thomas, B.C.; Banfield, J.F., (2013). Short-read assembly of full-length 16S amplicons reveals bacterial diversity in subsurface sediments. *PloS one* 2013: 8(2):e56018.
- Leelakriangsak, M.; Borisut, S., (2012) Characterization of the decolorizing activity of azo dyes by *Bacillus subtilis* azoreductase AzoR1. *Song. J. Sci. Technol.*, 34 (5): 509-516.
- Moosvi, S.; Kher, X.; Madamwar, D., (2007). Isolation, characterization and decolorization of textile dyes by a mixed bacterial consortium JW-2. *Dyes Pigm.*, 74: 723–729.
- Ogunjobi, A.A.; Oyinloye, I.A.; Sanuth, H.A., (2012). Bioremediation of effluent from local textile industry using *Bacillus licheniformis*. *N.Y. Sci. J.*, 5(12): 29-33.
- Olukanni, D.O.; Osuntoki, A.A.; Awotula, A.O.; Kalyani, D.C.; Gbenle, G.O.; Govindwar, S.P., (2013). Decolorization of dye house effluent and biodegradation of Congo Red by *Bacillus thuringiensis* RUN1. *J.M.B.*, 23(6): 843-84.
- Pandey, A.; Singh, P.; Iyengar, L., (2007). Bacterial decolourisation and degradation of azo dyes. *Int. Biodeterio. Biodegrad.*, (59): 73-84.
- Prasad, A.S.; Bhaskara, K.V., (2010). Physico-chemical characterization of textile effluents and screening for dye decolourizing Bacteria. *Global J. Biotechno. Biochem.*, 5 : (2): 55-62.
- Rajamohan, N.; Karthikeyan, C., (2004). Fungi Biodegradation of Dye house Effluent and Kinetic Modeling' Department of Chemical Engineering, Annamalai University, Annamalainagar, Tamilnadu-India.
- Rajeswari, M.; Bhuvanewari, V., (2016). Production of extracellular laccase from the newly isolated *Bacillus* sp. PK4. *Afr. J. Biotechno.*, 15(34): 1813-1826.
- Salisu, D.; Mustapha, H.B., (2010). Industrial Pollution and Implication on Source of Water Supply in Kano, Nigeria. *Int. J. Eng. Technol.*, 10: 1-32.
- Samuel, E.A.; Ayobami, O. A., (2011). Evaluation of microbial system for bio-treatment of textile waste effluent in Nigeria. *Biodecolourisation and Biodegradation of textile dye. JASEM.*, 15(1): 79-86.
- Saratale, R.G.; Saratale, G.D.; Kalyani, D.C.; Chang, J.S.; Govindwar, S.P., (2009). Enhanced decolorization and biodegradation of textile azo dye Scarlet R by using developed microbial consortium-GR. *Bioresour. Technol.*, 100: 2493-2500.
- Saratale, R.G.; Saratale, G.D.; Chang, J. S.; Govindwar, S.P., (2011). Bacterial decolorization and degradation of azo dyes: a review. *J. Taiwan Inst. Chem. Eng.*, 42:138-157.

- Shah, M.P., (2018). Bioremediation-Wastewater Treatment. *J. Bioremediat. Biodegrad.*, 9: 427.
- Singh, G.; Ahuja, N.; Sharma, P.; Capalash, N., (2009). Response surface methodology for the optimized production of an alkalophilic laccase from γ -proteobacterium JB. *BioRes.*, 4(2): 544-553.
- Singh, R.P.; Singh, P.K.; Singh, R.L., (2014). Bacterial Decolorization of textile azo dye Acid Orange by *Staphylococcus hominis* RMLRT03. *Toxicol. Int.*, 21:160-166.
- Sondhi, S.; Sharma, P.; George, N.; Chauhan, P. S.; Puri, N.; Gupta, N., (2014). An extracellular thermo-alkali-stable laccase from *Bacillus tequilensis* SN4, with a potential to biobleach softwood pulp. *3 Biotech.*, 5(2): 175-185.
- Srinivasan, V.; Bhavan, S.P.; Krishnakumar, J., (2014). Bioremediation of textile dye effluent by *Bacillus* and *Pseudomonas* spp. *Int. J. Sci. Environ. Techn.*, 3(6): 2215-2224.
- Sriram, N.; Reetha, D.; Saranraj, P., (2013). Biological Degradation of Reactive Dyes by Using Bacteria Isolated from Dye Effluent Contaminated Soil. *Middle-East J. Sci. Res.*, 17(12): 1695-1700.
- Usman, D.H.; Ibrahim, A.; Abdullahi S., (2012). Potentials of Bacterial isolates in Bioremediation of Petroleum Refinery and effluent Wastewater. *J. Appl. Phytotechn. Environ. Sanit.*, 1(3): 131-138.
- Vigneshpriya, D; Shanthi, E., (2015). Physicochemical characterization of textile wastewater. *Int. J. Innov. Res. Develop.*, 4(10): 236.
- Yaseen, D.A.; Scholz, M., (2017). Comparison of experimental ponds for the treatment of dye wastewater under controlled and semi-natural conditions. *Environ. Sci. Poll. Res.*, 24(19): 16031-16040.
- Wang, F.; Yao, J.; Si, Y.; Chen, H.; Russel, M., (2010). Short time effect of heavy metals in soil microbes. *Soil Microb. Biochem.*, 41: 2031-2037.

Comparison Of Physical And Physiological Parameters Of Children Skier And Volleyball Players

Neşe Akpınar Kocakulak ^{*1} , Yahya Polat ^{*2} , Zuhâl Hamurcu ^{*3} , Osman Pepe ^{*2} ,
Bekir Çoksevîm ^{*4} 

Abstract

This study purpose; to compare the athletic performance of the physical and physiological characteristics of the children who are in the age of 10-15 years and who have regular skiing, with the same characteristics of the children of the same age group and who have played volleyball for one year. Work group; ages 10-15 between changing and over a year volleyball playing 24 girls with same age group the and regular ski sport who 15 girl child volunteer participation with created. Methods; volunteers participating in research lengths naked standing with height measuring instrument and body weights were measured with the weighbridge (Premier). Body oil the percentage determination for; measurements were taken from 6 regions with skinfold caliper (Holtain LTD. Crymych U.K.) and body fat percentages were calculated according to Lange formula. Right-left hand gripping forces hand dynamometer (Takei Hand Grip) and FVC, VC, MW values were measured using spirometer (Cosmed, Pony Spirometer Graphic). Measurements of arterial systolic and diastolic blood pressures from the left arm of all volunteers were taken with the blood pressure monitor (Microfile BP-3AS1-2) and recorded in mmHg. Oxymeter saturation of the volunteers was measured using the Oximeter (NBP-40 Handheld). Resting and post-exercise heart rate, flexibility, speed, agility, long jump, endurance were evaluated by appropriate measurement methods. All data obtained from the measurements were evaluated using the Mann-Whitney U test. Significance levels of the difference between the groups were taken as 0.05. Findings; the body fat percentage (%) and exercise pulse of the athletes who played volleyball were higher than the skiers ($p = 0.002$). Long jump (anaerobic power), endurance (aerobic power) were found skiers kids higher than volleyball players ($p = 0.002$, $p = 0.029$) and flexibility was higher in children playing volleyball ($p = 0, 012$). No difference was found between the two groups in terms of speed, agility, right/left hand claw strength ($p > 0. 05$). There was no difference between lung function of the athletes who played volleyball and skiing ($p > 0. 05$). As a result of the special training methods and programs of skiing and volleyball branches while the strength and flexibility characteristics of the volleyball players were improved, it was observed that the strength and durability properties of the skiers were better.

Keywords

Skiing, volleyball, physical and physiological development

¹ Izmir Democracy University, Faculty of Health Sciences, Department of Sport Sciences, 35140, Izmir, Turkey

² Erciyes University, Faculty of Sport Sciences, Talas/Kayseri

³ Erciyes University, Faculty of Medicine, Department of Medical Biology, Talas/Kayseri

⁴ Erciyes University, Faculty of Medicine, Department of Physiology, Talas/ Kayseri

*Corresponding Author: nese.kocakulak@idu.edu.tr

Manuscript received date: December 18, 2018

Accept Date: December 31, 2018

Published Date: December 31, 2018.

1. INTRODUCTION

Besides to body compositions of athletes both in individual and team sports, sports sciences evaluate physical and physiological profiles among intensive research areas. Every healthy person has the ability to move. However, the ability to develop this ability is different. In addition to the structural quality, which determines the extent of development, the support of this feature from a very early age through training, the quality of the training and the nature of the sport branch constitute the basis of the

increasing sporting success. Physical health acquired during childhood and adolescence is essential for the body to function optimally (1). Physical activity during childhood is an important factor to consider in terms of maintaining normal growth and development (2). Regular physical activity has extremely positive effects on children's bodies and minds. At the same time, it is stated that the child gains the habit of using their free time in a positive and beneficial way and contributes to the child's learning capacity, social, emotional and perceptual motor development and physical fitness (3). Skiing is a sport that requires complex and special skills. If the ski is defined simply, after the appropriate costume, equipment and training; flat planks with curved ends attached to the feet and guided bars for guiding and balancing; The hill has a layout which aims to reach from point downwards on the abdomen without falling down. One of the most important sports that increases awareness in children is skiing. When skiing, each part of the body should be managed separately and kept under control. The physical awareness of the beginners at an early age is higher than the other children. In addition to physical awareness, their awareness about themselves increases. They self-discover their strengths and weaknesses and learn how to manage them. In contrast to other sports, there is little research on the physical and physiological characteristics of skiers both in the world and in our country (4). Many individual and team sports require a combination of physical, technical, tactical and mental skills. The players have to have many features such as aerobic and anaerobic capacities in order to perform fast, strong and continuous movements. Volleyball players should also have such characteristics. Team sports require a detailed skill, including physical, technical, mental and tactical aspects. Among them, the physical skills of the players significantly affect the game intelligence and team tactics because ball games require repeated maximum effort. Therefore, players must have physical skills to strengthen their aerobic and anaerobic capacities and to ensure long-term attack and defense efficiency in order to perform fast and hard movements. Such physical skills are very important when playing volleyball (5). Volleyball is an interval sport consisting of short-term load and rest stages. Volleyball also includes sequential, aerobic and anaerobic loading. Therefore, it can be thought that it requires high muscle strength and skill (6). In order for players to perform fast and powerful movements, they must have many physical and physiological features such as aerobic and anaerobic capacities. Volleyball players must also have such characteristics. Volleyball is one of the most popular branches in the world and it is stated that there are more than 800 million people who play volleyball at least once a week. Volleyball sport; short-term exercise periods and "interval", which can be changed with rest, can be defined as a sport (7). The physical and physiological features required by this sport have a very important place in success. Sports science, therefore as well as the physiological profile of athletes, body composition, physical and physiological profiles are evaluated among the intensive research areas.

The purpose of this study is; the physical and physiological characteristics of children skiing between 10-15 years of age, the athletic performance of the same age group and the same characteristics of children playing volleyball for a year is to compare.

MATERIALS & METHODS

The research between the ages of 10-15 and volleyball for a year 15 skiers who have been skiing in alpine discipline for year with 24 volleyball children who have been playing participated voluntarily. The physical and physiological capacities the volunteers were evaluated using the following measurement methods. Volunteers participating in research lengths naked standing with height measuring instrument and body weights were measured with the weighbridge (Premier). For determination of body fat percentage; The skinfold caliper (Holtain LTD. Crymych U.K.), which measures the thickness of the subcutaneous fat with thickness between 1-39 mm, it was measured in 6 regions and body fat percentages were calculated according to the Lange formula (8). Right-left hand gripping forces hand dynamometer (Takei Hand Grip) and FVC, VC, MW values were measured using spirometer (Cosmed, Pony Spirometer Graphic). Measurements of arterial systolic and diastolic blood pressures from the left arm of all volunteers were taken with the blood pressure monitor (Microfile BP-3AS1-2) and recorded in mmHg. Oxymeter saturation of the volunteers was measured using the Oximeter (NBP-40 Handheld). Resting and post-exercise heart rate, flexibility, speed, agility, long jump, endurance were evaluated by appropriate measurement methods. (9,10,11).

Statistical Evaluation: All data obtained from the measurements were evaluated statistically using nonparametric test, Mann-Whitney U test. Significance levels of the difference between the groups were taken as 0.05.

FINDINGS

Table 1 shows the physical and physiological characteristics of skiers and volleyball players. Physical properties of body fat ratio, volleyball players were significantly higher than skiers ($p=0.002$). Physiological characteristics of the heart rate after exercise was found more volleyball players than skiers. No statistically significant difference was found between skiers and volleyball players in terms of resting heart rate, systolic and diastolic blood pressure and oxygen saturation ($p>0.05$).

Table 2 shows the athletic performance values of skiers and volleyball players. Long jump (anaerobic power), endurance (aerobic power) were found skiers kids higher than volleyball players ($p=0.05$) and flexibility was higher in children playing

volleyball (p>0.05). No difference was found between the two groups in terms of speed, agility, right/left hand claw strength (p>0.05).

Table 1. Comparison of physical and physiological characteristics of athletes playing volleyball and skiing.

Parameters	Parameters Volleyball Players (n=24)	Skiers (n=15)	P and Z Values
Age (year) (avg ± SS)	12.37 ± 1.13	12.37 ± 1.13	p = 0.109 Z = 1.601
Length (cm) (avg ± SS)	155.00 ± 8.93	150.73 ± 9.75	p = 0.241 Z = 1.172
Weight (kg) (avg ± SS)	42.58 ± 6.68	41.40 ± 6.92	p=0.514 Z =0.653
Body Fat Ratio (%) (avg ± SS)	15.60 ± 8.83	11.04 ± 4.28	*p = 0.002 Z = 3.046
Resting Pulse (stroke/min) (avg ± SS)	77.00 ± 9.72	75.40 ± 11.59	p = 0.874 Z = 0.159
Exercise Pulse (stroke/min) (avg ± SS)	111.04 ± 13.33	92.87 ± 11.83	p = 0.000 Z = 0.029
Systolic Blood Pressure (mmhg) (avg ± SS)	110.46 ± 16.28	110.33 ± 17.06	p = 0.977 Z = 0.029
Diastolic Blood Pressure (mmhg) (avg ± SS)	74.79 ± 12.01	68.47 ± 17.06	p = 0.080 Z = 1.750
Oxygen Saturated (%) (avg ± SS)	97.75 ± 1.26	97.93 ± 0.80	p = 0.603 Z = 0.520

Mann Whitney U test /*p<0.05

*Body fat percentage and exercise rate of volleyball players were found higher than skiers (p=0.002).

Table 2. Comparison of athletic performance values of volleyball players and skiers.

Parameters	Volleyball Players (n=24)	Skiers (n=15)	P and Z Values
Flexibility (CM) (avg. Tss)	22.58 ± 5.27	18.13 ± 4.21	*p = 0.012 Z = 0.517
Speed 50 m (avg. Tss)	10.14 ± 0.64	10.18 ± 0.62	p = 0.618 Z = 0.505
Agility (avg. Tss)	3.86 ± 1.45	3.81 ± 0.83	p = 0.977 Z = 0.029
Long Jump (cm) (On.Tss)	134.04 ± 9.97	143.73 ± 42.27	p = 0.002 Z = 3.092
Right Grip (KgW) (avg. ±SS)	8.85 ± 3.80	8.53 ± 3.36	*p = 0.165 Z = 1.390
Left Grip (KgW) (avg. ± SS)	7.26 ± 4.07	8.53 ± 3.36	p = 0.200 Z = 1.282
Durability (avg. Tss)	1566.67 ± 502.75	1973.33 ± 481.76	*p = 0.029 Z = 2.181

Mann Whitney U test /*p<0.05 <0.05

*It was found that volleyball players were more flexible than skiers and skiers had better aerobic and anaerobic capacity than volleyball players.

Table 3. Comparison of lung function of athletes playing volleyball and skiing.

Parameters	Parameters Volleyball Players (n=24)	Skiers (n=15)	P and Z Values
FVC (avg ± SS)	2.74 ±0.61	2.60±0.52	p = 0.279 Z = 1.083
VC (avg ± SS)	2.45 ± 0.55	2.48 ±11.83	p = 0.809 Z = 0.462
MW(avg ± SS)	79.94 ± 21.74	79.11 ± 16.75	p=0.658 Z =0.462
Anaerobic Power (avg ± SS)	23.58 ±5.71	27.67 ±5.12	p = 0.066 Z = 1.839

2. Results

Regular physical activity from childhood, making exercise an indispensable part of daily life, increasing the amount of daily physical activity over time is very important in protecting individual health and reducing the health risks to be encountered old age (12). Motor development is parallel to the development of physical growth and central nervous system. It is a process that starts before birth and continues throughout life and is fundamental to physical activity. Physical activity is the most important issue to be considered in the growth process of children. However, it is well known that today's children do less physical activity than recommended (13). In our study, there was no difference in body weight between the two groups, while body fat ratio was higher in volleyball players than in skiers. Body weight and body fat percentages of basketball players and volleyball players were compared, there was no difference in body weight between the two groups, while body fat percentage was found to be higher in volleyball players (14). While all information is in parallel with each other, body fat content in volleyball players is high in the restricted movement area, rest periods are longer according to the branches, and the body fat rate is thought to be high because the used energy sources do not allow the use of fat.

It is stated that the heart rate is higher in volleyball players after exercise and it is stated that the pulse, which is an important indicator of physical adaptation, is not better in volleyball players than in skiers.

In the literature comparing volleyball and handball players, volleyball players are reported to have higher flexibility levels (15). Flexibility of volleyball players; volleyball game, rust, service throw, the ball to the opponent area, the need for flexibility, such as the ability to place the defense is due to the need. It is believed that the speed provided by a static balance on skiing affects the flexible capability. In our studies, volleyball players were found to be more flexible than skiers.

In our study, the strength test showing the anaerobic power with long jump and aerobic strength was found higher in skiers than in volleyball players. The success of some skiers in the alpine discipline and their aerobic capacities have shown a strong relationship between the training and the necessary energy during the race is met with a great deal of aerobic capacity (15). Although aerobic power is important in alpine discipline, it is stated that it does not distinguish between skiers at various levels and it is important in skiing in anaerobic power (16,17). In our findings, the high level of aerobic and anaerobic capacities skiers according to volleyball players is in parallel with the literature findings.

As a result of the special training methods and programs of the skiing and volleyball branches, the quick strength and flexibility characteristics of the volleyball players were improved and the strength and durability of the skiers were better.

References

1. Baltacı, G. Çocuk ve Spor. Klasman Matbaacılık, Sağlık Bakanlığı, Yayın no:730, 2008. Ankara.
2. Erceg, M., Zagorac, N., Katic, R. The impact of football training on motor development in male children. Coll Antropol, 32: 241-7, 2008.
3. Abigail. F., John, J., Loise, A., Colette, M. Fundamental movement skills and habitual physical activity in young children
4. Neumary G, Hoemagl H, Pfister R ve ark. Physical and physiological factors associated with success in professional alpine skiing. International Journal of Sports Medicine, 24: 571-575, 2003.

5. Sozen, H. The effect of volleyball training on the physical fitness of high school students *Procedia - Social and Behavioral Sciences*, 46, 1455 – 1460, 2012.
6. Tsunawake, N., Tahara, Y., Moji, K. Body composition and physical fitness of female volleyball and basketball players of the japan inter-high school championship teams. *J Physiol Anthropol Appl Human Sci*, 22, 195-201, 2003.
7. Abreu, T., Almeida, D., Soares, EA. Nutritional and anthropometric profile of adolescent volleyball athletes. *Revista Brasileira de Medicina do Esporte*, 9:4, 2003.
8. Smith DJ, Roberts D, Watson B. Physical, physiological and performance differences between Canadian national team and universiade volleyball players. *Journal of Sports Science*, 10: 131-8, 1992.
9. Zorba, E., Ziyagil, MA. Vücut kompozisyonu ve ölçüm metotları. Sayfa: 299, *Erek Ofset*, Trabzon, 1995. 10. Smith N., *J. Sports Medicine: Health care for young athletes*. sayfa: 32-74, 1983.
11. Tamer, K. Sporda fiziksel-fizyolojik performansın ölçülmesi ve değerlendirilmesi *Bağırhan yayınevi-Ankara*, sayfa: 27-154, 2000.
12. Cicioğlu, I., Günay, M., Gökdemir, K. Farklı branşlardaki elit bayan sporcuların fiziksel ve fizyolojik parametrelerinin karşılaştırılması. *Gazi Beden Eğitimi ve Spor Bilimleri Dergisi* 3: 9-16, 1998.
13. Toivo, J., Growth, J. J. (2000) *Physical activity, and motor development in prepubertal children*, CRC Press, 51–55.
14. Tsunawake, N., Tahara, Y., Moji, K et al. Body composition and physical fitness of female volleyball and basketball players of the japan interhigh school championship teams. *J Physiol Anthropol Appl Human Sci*, 22: 195-201, 2003.
15. White, A.T., Johnson, S.C. Physiological aspects and injury in elite Alpine skiers. *Sports Med*, 15: 170-8, 1993.
16. Maffiuletti, N.A., Impellizzeri, F., Rampinini, E, et al. Is aerobic power really critical for success in alpine skiing. *International Journal of Sports Medicine*, 27: 166-167, 2006.
17. Andersen, R.E., Montgomery, D.L. Physiology of alpine skiing. *Sports Med*, 6: 210-21, 1988

Synthesis and Characterization of Metal Carbonyls [$M(CO)_6(M = Cr, Mo, W)$] with Indole -3-carboxyaldehydemethanesulfonylhydrazone

Sema SERT ^{*1} , Ümmühan ÖZDEMİR ÖZMEN ² 

Abstract

Four new complexes, $[M(CO)_5(msh4)](Cr(1), Mo(2), W(3))$, and $Re(CO)_4Br(inmsh)(4)$, were synthesized by the photochemical reaction of metal carbonyls with indole-3-carboxyaldehydemethanesulfonyl hydrazone (inmsh) and characterized by using elemental analysis, 1H NMR, EI-MS and IR spectra. The spectroscopic studies show that inmsh behaves as a monodentate ligand coordinating via imine N donor atom in $[M(CO)_5(inmsh)](M = Cr, Mo, W)$ and $Re(CO)_4Br(inmsh)$.

Keywords

Sulfonylhydrazones, Metal Carbonyls, Photochemical Reactions.

¹ Ege Üniversitesi, Fen Fakültesi, Kimya Bölümü, Bornova, İzmir, TÜRKİYE

² Gazi Üniversitesi, Fen-Edebiyat Fakültesi, Kimya Bölümü, Teknikokullar, Ankara, TÜRKİYE

*Corresponding Author: semasertkimya@hotmail.com

Manuscript received date: September 24, 2018

Accept Date: November 28, 2018

Published Date: June 30, 2019.

1. INTRODUCTION

The sulfonamides ($-SO_2NH-$) are used widely as antibacterial agents because of their lower cost, lower activity and most activity against bacterial diseases[1]. Sulfo drugs are used as chemotherapeutic agents with large spectrum of activity and they are used today for various bacterial, protozoal and fungal infections[2a,b]. Methane sulfonamide derivatives possess DNA-binding ability and show cytostatic effects which have usage in cancer chemotherapy. Sulfonylhydrazones derived from sulfonamides have pharmacological properties as antibacterial, antitumor, diuretic, antiviral, antinociceptive activity and enzyme inhibition especially to carbonic anhydrase species[3,4]. Many of the physiologically active hydrazones have applications in the treatment of illness like tuberculosis, leprosy and mental damage.

The Schiff base metal carbonyl complexes have continued to attract attention in part because of the different possible coordination geometries which the ligand may adopt[5-7]. Their low energy metal-to-ligand charge transfer transitions make these molecules attractive for luminescence and electron transfer reactions[8]. Several of these complexes have been shown to be effective catalysts in allylic alkylation reactions[9,10]. Chiral metal complexes have been employed for stereoselective organic transformations.

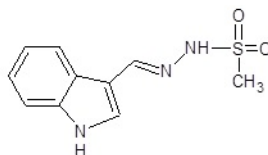


Figure 1. inmsh (indole-3-carboxyaldehydemethanesulfonylhydrazone)

In this article, four new complexes $[M(CO)_5(inmsh)]$ (1-3) and $[Re(CO)_4Br(inmsh)]$ (4) have been synthesized by the photochemical reaction of metal carbonyls $M(CO)_6(M = Cr, Mo, W)$ with indole-3-carboxyaldehydemethanesulfonylhydrazone (inmsh).

2. EXPERIMENTAL SECTION

All preparation were carried out under dry nitrogen using Schlenk techniques. All solvents used in the synthesis were deoxygenated. Microanalyses of C, H, N and S were performed with a Leco-CHNS-0-9320 elemental analyzer by the Technical and Scientific Research Council of Turkey, TUBITAK. FTIR spectra were recorded on samples in hexane at Ege University on a Mattson 1000 FT spectrophotometer. ^1H NMR spectra were recorded in DMSO on a 400 MHz FT-NMR at TUBITAK. Electron impact mass spectroscopy were recorded on a Micromass VG Platform-II LC-MS at TUBITAK. UV irradiations were performed with a medium-pressure 400W mercury lamp through a quartz-walled immersion well reactor.

Hexane, pentane, benzene, dichloromethane, acetone, ethyl alcohol, diethyl ether, silica gel and hydrazine hydrate were purchased from Merck. $M(CO)_6(M = Cr, Mo, W)$ and $Re(CO)_5Br$ were purchased from Aldrich. These reagents were used as supplied. Inmsh was prepared the literature method[11].

The complexes (1-4) were prepared by the photochemical reactions of metal carbonyls $M(CO)_6(M = Cr, Mo, W)$ and $Re(CO)_5Br$ with inmsh were obtained in 70-80% yields by similar methods of which the following is typical.

$Cr(CO)_6$ (0.44 g, 2 mmol) and inmsh (0.48 g, 2 mmol) were dissolved in tetrahydrofuran (80-100 mL). The solution was irradiated for 2 hr at room temperature. During the irradiation, the color of the reaction mixture changed from colorless to dark yellow. After the irradiation, the reaction mixture was evaporated under vacuum, yielding a dark yellow solid. After dissolving in dichloromethane (10 mL), 50 mL of petroleum ether was added, resulting in the precipitation of a dark yellow solid, which was washed with petroleum ether and dried under vacuum. Yield of $Cr(CO)_5(\text{inmsh})$: 80%

3. RESULTS AND DISCUSSION

Complexes 1-4 were prepared by a photochemical reaction as shown in Scheme 1. The photogeneration of $M(CO)_5$ from $M(CO)_6(M = Cr, Mo, W)$ has been studied extensively. The 16-electron $M(CO)_5$ fragments react quickly with any available donor atom to form a $M(CO)_5L$ species [12,13]. In this study, photochemical reactions of $M(CO)_6(M = Cr, Mo, W)$ and $Re(CO)_5Br$ with inmsh gave a series of complexes 1-4 via CO displacement.

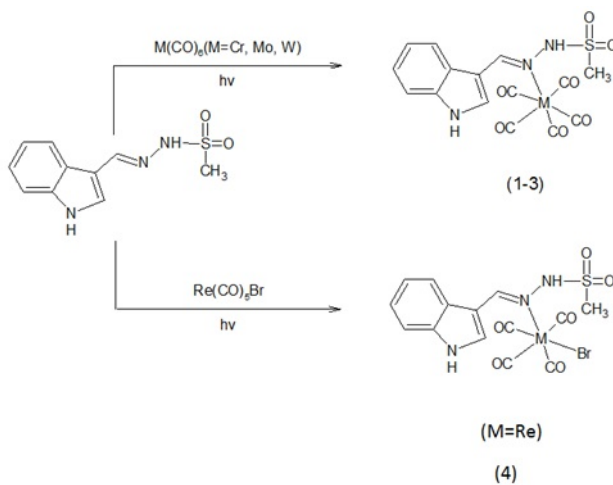


Figure 2. Photochemical reaction of metal carbonyls with the inmsh ligand.

The rather strong C=N stretching vibration, found at 1628 cm^{-1} in free inmsh shift to lower wave numbers in 1-4, showing that inmsh coordinates to the metal via the imine donor atom [14]. This shift has been explained as a weakening of the CN bond resulting from loss of electron density from the nitrogen to the metal atom. No shift was observed for the $\nu_{as}(SO)_2$, $\nu_{sym}(SO)_2$, and $\nu(NH)$ stretching vibrations on complex formation, showing that SO_2 and NH were not coordinated to metal atom in 1-4.

The number of carbonyl bands in the complexes provides important clues to the environment around the metal centers[15]. Five carbonyl stretching bands in 1-3 are attributed to local C_s symmetry of $M(CO)_5$. Similarly, four CO stretching absorptions in 4 indicates local C_{2v} symmetry (shown in Scheme 1).

In the ^1H NMR spectra of 1-4, NH proton of the free ligand at 10.01 ppm remains approximately unchanged in the complexes and shows that the NH group does not participate in coordination. Small shift to upfield for the imine peak may be related to a decrease in π -electron density in the C=N bond with complex formation in 1-4. According to these data, inmsh behaves as monodentate ligand with imine nitrogen atom in 1-4.

The mass spectral data of 1-4 show fragmentation via successive loss of CO groups and organic ligands.

In summary, indole-3-carboxyaldehydemethanesulfonylhydrazone behaves as monodentate ligand via the N imine donor atom in 1-4. IR and NMR spectra of the compounds show that the inmsh ligand coordinates to the metal atom for compounds

1-4 only via an imine N donor atom behaving as a monodentate neutral ligand. Also CN stretching vibrations in the IR spectra of the compounds shift to lower wave numbers, showing that the imine N donor atom coordinates to the central metal atom in compounds 1-4.

Cr(CO)₅(inmsh) (1): Yield: 80%. IR(KBr): 3190(s, ν NH), 1610(m, ν C=N), 1318(s, $\nu_{as}(SO)_2$), 1157(s, $\nu_{sym}(SO)_2$), 2070(m, $\nu(CO)$), 1970(m, $\nu(CO)$), 1947(s, $\nu(CO)$), 1935(s, $\nu(CO)$), 1872(m, $\nu(CO)$); ¹H NMR (400 MHz, DMSO-*d*₆): δ =12.96(s, 1H, *NH*_{ring}), 9.92(s, 1H, NH), 8.06(s, 1H, HC=N), 3.06(s, 3H, CH₃); EIMS m/z 444(10)[M⁺], 416(20)[M⁺-CO], 388(25)[M⁺-2CO], 360(30)[M⁺-3CO], 332(15)[M⁺-4CO], 304(20)[M⁺-5CO]; Anal.Calcd. for C₁₆H₁₄CrO₇N₃S (444.14 g/mol): calcd. C, 43.26; H, 3.15; N, 9.45; S, 7.21; found C, 43.52; H, 3.22; N, 9.56; S, 7.12.

Mo(CO)₅(inmsh) (2): Yield: 77%. IR(KBr): 3190(s, ν NH), 1610(m, ν C=N), 1317(s, $\nu_{as}(SO)_2$), 1158(s, $\nu_{sym}(SO)_2$), 2068(m, $\nu(CO)$), 1971(m, $\nu(CO)$), 1946(s, $\nu(CO)$), 1926(s, $\nu(CO)$), 1873(m, $\nu(CO)$); ¹H NMR(400 MHz, DMSO-*d*₆): δ =12.98(s, 1H, *NH*_{ring}), 9.92(s, 1H, NH), 8.06(s, 1H, HC=N), 3.00(s, 3H, CH₃); EIMS m/z 460(10)[M⁺-CO], 432(15)[M⁺-2CO], 404(20)[M⁺-3CO], 361(30)[M⁺-4CO-Me], 252(25)[inmsh]; Anal.Calcd.for C₁₆H₁₄MoO₇N₃S (489.09 g/mol): calcd. C, 39.37; H, 2.87; N, 8.60; S, 6.56; found C, 39.20; H, 2.98; N, 8.48; S, 6.46.

W(CO)₅(inmsh) (3): Yield: 74%. IR(KBr): 3190(s, ν NH), 1609(m, ν C=N), 1318(s, $\nu_{as}(SO)_2$), 1156(s, $\nu_{sym}(SO)_2$), 2069(m, $\nu(CO)$), 1970(m, $\nu(CO)$), 1930(s, $\nu(CO)$), 1920(s, $\nu(CO)$), 1878(m, $\nu(CO)$); ¹H NMR(400 MHz, DMSO-*d*₆): δ =12.96(s, 1H, *NH*_{ring}), 9.96(s, 1H, NH), 8.04(s, 1H, HC=N), 3.01(s, 3H, CH₃); EIMS m/z 561(25) [M⁺-Me], 533(20)[M⁺-Me-CO], 505(20)[M⁺-Me-2CO], 477(20)[M⁺-Me-3CO], 449(20)[M⁺-Me-4CO]; Anal.Calcd.for C₁₆H₁₄WO₇N₃S (576 g/mol): calcd. C, 33.33; H, 2.43; N, 7.29; S, 5.55; found C, 33.86; H, 2.48; N, 7.76; S, 5.40.

Re(CO)₄Br(inmsh) (4): Yield:76%. IR(KBr): 3190(s, ν NH), 1608(m, ν C=N),1318(s, $\nu_{as}(SO)_2$), 1159(s, $\nu_{sym}(SO)_2$), 2110(w, $\nu(CO)$), 2022(m, $\nu(CO)$), 1950(m, $\nu(CO)$), 1942(m, $\nu(CO)$); ¹H NMR(400 MHz, DMSO- *d*₆): δ =12.94(s, 1H, *NH*_{ring}), 9.94(s, 1H, NH), 8.04(s, 1H, HC=N),3.07(s, 3H, CH₃); EIMS m/z 602(15)[M⁺-CO], 574(30)[M⁺-2CO], 546(35) [M⁺-3CO], 518(10) [M⁺-4CO]; Anal.Calcd.for C₁₅H₁₄O₆N₃ReSBr (630.25 g/mol): calcd. C, 28.58; H, 2.22; N, 6.66; S, 5.08; found C, 28.38; H, 2.18; N, 6.80; S, 5.28.

Spectroscopic data of free ligand “inmsh”(take from lit.[11]): IR(KBr): 3190(s, ν NH), 1628(m, ν C=N), 1317(s, $\nu_{as}(SO)_2$), 1157(s, $\nu_{sym}(SO)_2$) ; ¹H NMR(400 MHz, DMSO): δ =12.99(s, 1H, *NH*_{ring}), 10.01(s, 1H, NH), 8.36(s, 1H, HC=N), 3.08(s, 3H, CH₃).

Acknowledgement

We thank BP for the provision of photochemical apparatus and the Research Foundation of Ege and Gazi University. We thank TÜBİTAK for all allocation of time for NMR, mass spectra and elemental analyses.

REFERENCES

- [1] S.Özçelik, M.Dinçer, M.Şekerci, A.Balaban, Ü.Özdemir, Acta Crystallogr Sect.E 60:1552-1553(2004).
- [2] (a) H.Alyar, S.Alyar, A.Ünal, N.Özbek, N.Karacan, J.Mol.Struct 1028:116-125(2012); (b) H.Alyar, A.Ünal, N.Özbek, S.Alyar, N.Karacan, Spectrochim Acta A 98:329-336(2012).
- [3] N.I.Dodoff, Ü.Özdemir, N.Karacan, M.Georgieva, S.M.Konstantinov, M.E.Stefanova, Z.Naturforsch, 54:1553-1562(1999).
- [4]Ü.Özdemir, F.Arslan, F.Hamurcu, Spectrochim Acta A 75: 121-126(2010).
- [5] S.W.Kirtley, In Comprehensive Organometallic Chemistry, G.Wilkinson, F.G.A.Stone, E.W.Abel(Eds), p. 1079, Pergamon Press, Oxford (1982).
- [6]A.S.Cavallo, G.Solladie, E.Tsano, J. Organomet. Chem., 144, 181(1978).
- [7] R.Lal De, K.Samanta (nee Bera), I. Banerjee, Indian J. Chem., 40A,144(2001).
- [8] W. Kaim, S.Kohlmann, Inorg. Chem., 26, 68(1987).
- [9] B.M.Trost, M.Lautens, J. Am .Chem. Soc.,104, 5543 (1982); 105, 3343 (1982).
- [10] B.J.Brisdon, D.W.Brown, C.R.Wills, Polyhedron, 5, 439(1986).

- [11] A.B.Gündüzalp, Ü.Ö.Özmen, B.S.Çevrimli, S.Mamaş, S.Çete, Med. Chem. Res. 23:3255-3268(2014).
- [12] F.Sarıkahya, O.S.Şentürk, Synth. React. Inorg. Met.-Org. Chem., 31, 1843(2001).
- [13] F.A.Cotton, G.Wilkinson, Advanced Inorganic Chemistry, 5th Ed.1047(1988).
- [14] J.E.Kovacic, Spectrochim.Acta 23A,183(1967).
- [15] G.L.Miedler, D.A.Tarr, Inorganic Chemistry, 2nd Ed.,471(2000).